REALIZATION OF HIGH-FIDELITY TWO-QUBIT GATES WITH A TUNABLE COUPLER FOR FLUXONIUM QUBITS

Master Thesis

To obtain the degree of Master in Science

at the Delft University of Technology, the Netherlands

by

Siyu WANG

A thesis submitted in partial fulfillment of the requirements for the degree of Master of in Applied Physics

Defense committee:	Prof. Dr. Leonardo DiCarlo
	Prof. Dr. Maximilian Rimbach-Russ
	Prof. Dr. Christian Kraglund Andersen
	Figen Yilmaz
Supervisors:	Prof. Dr. Christian Kraglund Andersen
	Figen Yilmaz
Project Duration:	December 2022 - Nov 2023
Student number:	5600162

ABSTRACT

Quantum gates play an indispensable role in quantum computing, serving as the foundation for executing efficient quantum algorithms. In particular, the development and optimization of two-qubit gates have emerged as a significant challenge in the field. In this work, we propose an innovative structure, termed as the FXTFX (fluxonium-transmon-fluxonium) system, leveraging a tunable transmon as the coupler for two fluxonium qubits to construct a two-qubit gate. Our FXTFX configuration demonstrates the capability to achieve a strong coupling strength between the coupler and fluxonium ($g/2\pi$ = 226 MHz), while maintaining the ZZ interaction below 10 kHz. Utilizing this setup, I designed and simulated the CZ gate and show through rigorous simulations that a gate time of 66 ns produces a high gate fidelity of 99.88%.

CONTENTS

1

INTRODUCTION

1.1. BACKGROUND

During the past decade, superconducting qubits have made great progress in gate fidelity, and have been a competitive candidate for building quantum computers [1]. Among various superconducting qubits, the transmon qubit stands out due to its widespread use [2]. Nevertheless, transmon qubits exhibit limited anharmonicity, which can enhance the leakage. Additionally, their high transition frequencies make them susceptible to dielectric losses[3].

Vladimir Manucharyan and his colleagues in the group of Michel Devoret introduced a novel fluxonium-based qubit[4], which has a relatively large anharmonicity. Besides, fluxonium qubits can exceed 1 ms for the coherence time[5]. Therefore, fluxonium qubits are becoming a competitive alternative to transmon qubits. With these advantages, researchers[4, 6] demonstrated the fidelity of single-qubit gate on fluxonium qubits has over 99.99%. However, as the field advances, the creation and optimization of two-qubit gates for fluxonium become essential. Previous efforts [7, 8] encountered challenges, such as ZZ interactions, which are unwanted and always-on interactions in quantum system. Recently, MIT[9] demonstrated the implementations of two-qubit gate on fluxonium qubits with the gate fidelity around 99.92 %.

In this thesis, we propose an approach: the Fluxonium-Transmon-Fluxonium (FXTFX) architecture to integrate the benefits of both the transmon and fluxonium qubits. After deriving the theoretical coupling strength, we can obtain a device design that meets the target coupling strength value. Simulations are carried out to evaluate that the ZZ interaction is below 10 kHz in the strong-coupling FXTFX configuration. Furthermore, by using Rabi Oscillations to excite $|101\rangle$ state to the $|111\rangle$ state, we successfully implemented the CZ gate with π phase accumulation and, achieved a simulated gate fidelity of 99.88% in 66 ns gate time.

1

1.2. OUTLINE

In Chapter 2, we discuss superconducting qubits. This includes an introduction to LC oscillators, an exploration of the transmon qubit, and an overview of the fluxonium qubit. Chapter 3 introduces the novel concept of using tunable transmon as a coupler between two fluxonium qubits. This chapter not only provides a mathematical breakdown of the circuit, but also explains the principles of the CZ gates in our device. The focus then shifts to device design and simulations in Chapter 4. Here, we provide a broad overview of the design process, starting from the foundational principles of the fluxonium qubit and resonator designs, and extending to the detailed simulation models. A large part of this chapter is dedicated to the design and simulation of the FXTFX device. Lastly, Chapter 5 presents and discusses the measurement results for the fabricated chip.

2

SUPERCONDUCTING QUBIT

Qubit can be regarded as the building blocks of a quantum computer. For a traditional computer, a bit is a basic unit for storing information; a quantum bit, similar to a bit, is the smallest unit for a quantum computer to represent digital information. Like the conventional computer, the quantum computer also encodes information digitally. The most rapidly developing and successful ways to realize qubit are using natural atoms and artificial atoms. Natural atoms are the most obvious candidates, like trapped ions[10–13] or neutral atoms[14–17]. In these systems, the qubit states are represented by different energy levels or internal degrees of freedom (e.g., electron spin states) of the atoms, which have been studied extensively over the past decade with a strong theoretical foundation. Another attractive point is that the interaction between natural atom qubits and environment is weak leading to long coherence time[14, 18]. However, stability requirements like the high vacuum and low-temperature environments and the complexity of individual control[19] limit the scalability of natural atom qubits, which makes it difficult to build large-scale quantum computers. Conversely, the artificial atom qubits we introduce in this chapter: superconducting qubits, can be easily integrated into a chip, allowing for better scalability[20] compared to natural atom qubits. Besides, artificial atom qubits can be designed based on specific requirements, making it possible to meet desired characteristics[2, 21–23].

2.1. LC OSCILLATORS

The principle of a superconducting qubit, lies in the quantum mechanical properties of superconducting circuits to realize the two-level quantum system, which can be achieved by quantizing the circuit.

Mentioning this, a natural starting point is to consider the *LC* circuit consisting of an inductor L and a capacitor C (Fig. 2.1a), and the angular frequency of the oscillations in

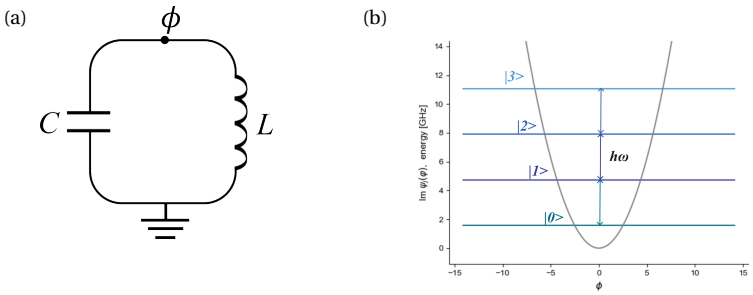

Figure 2.1: (*a*) Simple circuit diagram for a parallel $LC-$ oscillator. (*b*) Energy potential for the circuit, where energy levels are equidistantly spaced. This energy diagram was obtained through the Scqubits package [24].

the circuit is $\omega = \sqrt{\frac{1}{LC}}$. We now consider the electrical energy, named T, stored in the capacitor of the circuit, and the energy of the inductor in the magnetic field, called U. We can write down energy terms for the capacitor and inductor in terms of the node flux ϕ that is the flux through the inductor created by the current flow.

$$T = \frac{1}{2}C\dot{\phi}^2, \quad U = \frac{1}{2L}\phi^2 \tag{2.1}$$

We take the electrical energy as the kinetic energy and the inductive energy as the potential energy. The classical equations of motion in an LC circuit can be found from the Lagrangian $\mathscr{L}$, which is formulated as the difference between kinetic and potential energy terms[25].

$$\mathscr{L} = T - U = \frac{1}{2}C\dot{\phi}^2 - \frac{1}{2L}\phi^2 \tag{2.2}$$

With the Lagrangian of circuit, the generalized momenta Q, which is the magnitude of the charge on capacitor plates.

$$Q = \frac{\partial \mathscr{L}}{\partial \dot{\phi}} = C\dot{\phi} \tag{2.3}$$

The classical Hamiltonian of the system can be derived by using the Legendre transformation[26].

$$H = Q\dot{\phi} - \mathscr{L} = \frac{Q^2}{2C} + \frac{\phi^2}{2L} = \frac{Q^2}{2C} + \frac{1}{2}C\omega^2\phi^2 \tag{2.4}$$

This form is analogous to the mechanical harmonic oscillator Hamiltonian[27], which described in mass $m = C$, momentum $p = Q$ and position $x = \phi$.

$$H = \frac{p^2}{2m} + \frac{1}{2}m\omega^2 x^2 \tag{2.5}$$

Considering the analogy, quantization can be achieved simply by: the coordinate and its conjugate momentum can be promoted to quantum operators satisfying the commutation relation [28]:

$$[\hat{\phi}, \hat{Q}] = i\hbar \tag{2.6}$$

It is instructive to introduce the creation operator $\hat{a}^\dagger$ and the annihilation operator $\hat{a}$, which obey the commutation relation: $[\hat{a}, \hat{a}^\dagger] = 1$. The flux and charge operator can be expressed in terms of the creation and annihilation operators as[27]:

$$\hat{\phi} = \phi_{zpf}(\hat{a}^\dagger + \hat{a}), \quad \hat{Q} = iQ_{zpf}(\hat{a}^\dagger - \hat{a}) \tag{2.7}$$

with

$$\phi_{zpf} = \sqrt{\frac{L\hbar\omega}{2}} = \sqrt{\frac{\hbar}{2\omega C}}, \quad Q_{zpf} = \sqrt{\frac{C\hbar\omega}{2}} \tag{2.8}$$

the zero-point fluctuations of the flux and the charge variables, respectively.

With these definitions, we can rewrite the Hamiltonian as:

$$H = \frac{\hbar\omega}{2}(\hat{a}^\dagger\hat{a} + \hat{a}\hat{a}^\dagger) = \hbar\omega(\hat{a}^\dagger\hat{a} + \frac{1}{2}) \tag{2.9}$$

The eigenstate satisfies $\hat{a}^\dagger\hat{a}|n\rangle = n|n\rangle$[29], $n = 0, 1, 2, \ldots$, which means that the *LC* circuit produced discrete energy levels evenly spaced by $\hbar\omega$, as shown in Fig. 2.1b.

As mentioned, we want to implement a two-level system using superconducting circuits, usually achieved by choosing the eigenstate corresponding to the lowest two eigenenergies as the computational state. For the construction of a robust and reliable qubit, there must be a discernible energy difference between these two eigenstates. This distinction in energy levels facilitates a precise and distinct amount of energy necessary for transitions between the computational states, contributing to the control and manipulation of the qubit. The transition frequency of *LC* circuit is equal, which makes it impossible to use it to create and control qubits.

2.2. CHARGE QUBIT

In order to realize the addressable two-level system, nonlinearity can be introduced that requires a modification of the harmonic potential. To achieve this, we use the Josephson junction (JJ), the physics of which was first understood by Brian Josephson in 1962[30] and these junctions are widely used in the implementation of superconducting qubits such as charge[31, 32], flux[33, 34] and phase[35] qubits.

2.2.1. JOSEPHSON JUNCTION

Josephson junction is a non-linear and non-dissipative circuit element, which is constructed from two superconductors connected by an insulating barrier layer of appropriate thickness, typically 2-3 nm. Brian Josephson showed that the supercurrent through the barrier is:

$$I = I_c \sin\varphi \tag{2.10}$$

Here, φ is the phase difference between the phases of the two superconductors and I_c is the maximum supercurrent (Josephson current) that the junction can support[36] (the

critical current). Josephson also predicted that the time-dependent phase difference φ is related to the voltage V across the junction:

$$V = \frac{\phi_0}{2\pi}\frac{d\varphi}{dt} \tag{2.11}$$

with $\phi_0 = h/2e$ the magnetic flux quantum and φ can be described as $2\pi\phi(t)/\phi_0$, $\phi(t)$ is the flux introduced in Sec. 2.1. Taken Eq. (2.10) and Eq. (2.11) together is the Josephson relations. Applying the chain rule, the time derivative of the current can be obtained:

$$\frac{dI}{dt} = \frac{dI}{d\varphi}\frac{d\varphi}{dt} = \frac{2\pi I_c \cos\varphi}{\phi_0} V \tag{2.12}$$

Rearrange the above equation based on the form of the current-voltage relationship:

$$V = \frac{\phi_0}{2\pi I_c \cos\varphi}\frac{dI}{dt} = L(\varphi)\frac{dI}{dt} \tag{2.13}$$

This gives the expression of Josephson inductance[30]:

$$L(\varphi) = \frac{\phi_0}{2\pi I_c \cos\varphi} \tag{2.14}$$

As a result, the junction can be regarded as a non-linear inductor with inductance $L(\varphi)$, when below the critical current. Replacing the inductor L in the LC circuit with a JJ to introduce the nonlinearity can make the energy level no longer equally spaced.

The energy stored in capacitor and JJ can be derived by [27]:

$$\begin{aligned} H_J &= \int V(t)I(t)dt = \int I_c \sin(\varphi)\frac{\phi_0}{2\pi}\left(\frac{d\varphi}{dt}\right)dt \\ &= I_c\frac{\phi_0}{2\pi}\int \sin(\varphi)d\varphi = -E_J\cos(\varphi) \end{aligned} \tag{2.15}$$

$$H_C = \frac{(Q-Q_g)^2}{2C_\Sigma} = 4E_C(n-n_g)^2 \tag{2.16}$$

with $C_\Sigma = C_J + C_g$ the total capacitance, including both the self-capacitance C_J of JJ and the voltage V_g is coupled to the qubit island by a capacitance C_g, the charge number $n = Q/2e$. Defining $n_g = Q_g/2e$ to represent the effective offset charge of the external electric field bias[27], which can also be expressed as $n_g = C_g V_g/2e$, indicating the effect of the dimensionless gate voltage V_g[32].

Here E_J (Josephson energy) is the characteristic parameter of the junction and the capacitive element can be described as E_C (charging energy):

$$E_J = \frac{\phi_0 I_c}{2\pi}, \quad E_C = \frac{e^2}{2C_\Sigma} \tag{2.17}$$

In this case, the circuit Hamiltonian can be written by combining the charge energy and the Josephson energy contributions[38]:

$$H = 4E_C(n-n_g)^2 - E_J\cos(\varphi) \tag{2.18}$$

2.2.2. COOPER PAIR BOX AND TRANSMON

The nonlinearity introduced by JJ makes the Hamiltonian of the circuit non-degenerate, which allows us to realize an addressable two-level system to manipulate qubits. If the capacitance in the circuit is small, this is the typical regime for the charge qubit, also known as Cooper-pair box (CPB), where the Hamiltonian is dominated mainly by the charging energy E_C.

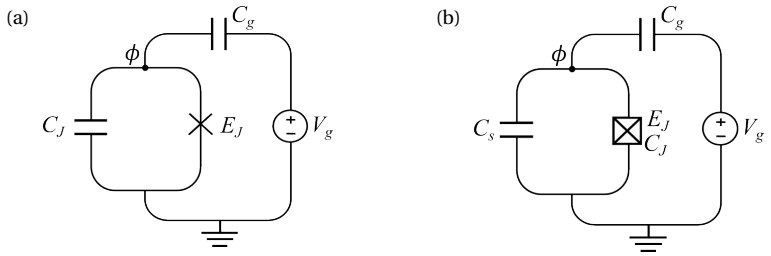

Figure 2.2: (*a*) CPB circuit. (*b*) Transmon. A pure Josephson junction tunneling element is represented as an "X". To simplify the schematic, the junction capacitance C_J is absorbed into the symbol of the Josephson tunneling element and is represented as a box with an "X" as shown in (*b*).

For a typical CPB, $E_J/E_C < 1$, the system's eigenenergies are highly sensitive to the offset charge n_g. However, increasing the E_J/E_C ratio can suppress the susceptibility to charge fluctuations exponentially and flatten the charge dispersion.

To access $E_J/E_C \gg 1$, one preferred method is by shunting the junction in the circuit with a large shunting capacitance, $C_s \gg C_J$, to lower the charging energy $E_C = e^2/2C_\Sigma$, $C_\Sigma = C_J + C_S + C_g$, commonly referred to as a transmon qubit circuit[2]. The transmon is operated in the regime $E_J/E_C \gtrsim 50$, in the limit, by expanding the $\cos(\phi)$ around 0 in Eq. (2.18) up to forth order[2], the eigenenergies E_m ($m \geq 0$) are given by:

$$E_m \simeq -E_J + \sqrt{8E_C E_J}(m + \frac{1}{2}) - \frac{E_C}{12}(6m^2 + 6m + 3) \tag{2.19}$$

$$E_{01} = \sqrt{8E_C E_J} - E_C, \quad E_{12} = \sqrt{8E_C E_J} - 2E_C, \quad \eta = -E_C/\hbar \tag{2.20}$$

E_{ij} is defined as the energy difference between eigenstates $|i\rangle$ and $|j\rangle$ and η is the anharmonicity.

This transmon regime enables the qubit transition frequency to be less sensitive to the charge noise, but this comes at the cost of the energy levels becoming more equidistant, which leads to reduce the anharmonicity η. This can lead to leakage, which is the quantum error process in that the qubit leaks out the preferred computational states to a state outside the computational subspace.

2.2.3. DC SQUID

In the superconducting circuit, one key element in controlling qubit control is the ability to tune the frequency of qubits. As we discussed in the previous section, the transmon

qubit frequency is determined by E_C and E_J, which can be tuned by changing its charging energy or Josephson energy. In comparison to E_C, E_J is usually selected for modification, by adding the direct current superconducting Quantum Interference Device (DC SQUID)[36].

2

DC SQUID consists of the superconducting loop with two Josephson junctions at both arms, shown in Fig. 2.3. By applying an external field, the external magnetic flux

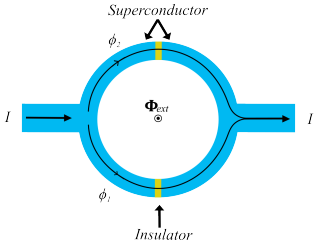

Figure 2.3: The schematic of DC SQUID with two Josephson junctions at both arms of the superconducting loop.

Φ_{ext} through the loop allows the Josephson Hamiltonian to be replaced by[2]

$$H_J = -E_{J1}\cos\phi_1 - E_{J2}\cos\phi_2 \tag{2.21}$$

$\phi_{1,2}$ represent the superconducting phase difference through junction 1 and 2 individually, then leads to the relationship[2]

$$\phi_1 - \phi_2 = 2\pi n + \frac{2\pi\Phi_{ext}}{\Phi_0} \tag{2.22}$$

with integer n. Defining the effective phase difference as $\phi = (\phi_1 + \phi_2)/2$ and $E_{J\Sigma} = E_{J1} + E_{J2}$ is the Josephson energy sum of the two Josephson junctions. Using the trigonometric identities, the Hamiltonian can be rewritten as

$$\begin{aligned} H_J &= -\frac{E_{J1}+E_{J2}}{2}\cos\left(\frac{\phi_1+\phi_2}{2}\right)\cos\left(\frac{\phi_1-\phi_2}{2}\right) + \frac{E_{J1}-E_{J2}}{2}\sin\left(\frac{\phi_1+\phi_2}{2}\right)\sin\left(\frac{\phi_1-\phi_2}{2}\right) \\ &= -E_{J\Sigma}[\cos\phi\cos\left(\frac{\pi\Phi_{ext}}{\Phi_0}\right) + d\sin\phi\sin\left(\frac{\pi\Phi_{ext}}{\Phi_0}\right)] \\ &= -E_{J\Sigma}\cos\left(\frac{\pi\Phi_{ext}}{\Phi_0}\right)\sqrt{1+d^2\tan^2\frac{\pi\Phi_{ext}}{\Phi_0}}\cos(\phi-\phi_0) \end{aligned} \tag{2.23}$$

where $d = \frac{E_{J2}-E_{J1}}{E_{J1}+E_{J2}}$ is the junction asymmetry, the phase ϕ_0 has the condition: $\tan\phi_0 = d\tan\left(\frac{\pi\Phi_{ext}}{\Phi_0}\right)$. As a result, the Josephson energy can be given by

$$E_J = E_{J\Sigma}\cos\left(\frac{\phi_e}{2}\right)\sqrt{1+d^2\tan^2(\frac{\phi_e}{2})} \tag{2.24}$$

Here, $\phi_e = 2\pi\Phi_{ext}/\Phi_0$.

2.2.4. TUNABLE TRANSMON

In a tunable transmon, the single Josephson junction of a regular transmon qubit we introduced above is replaced with a DC SQUID, see Fig. 2.4a. This combination imbues the transmon qubit with an additional degree of control: the qubit frequency, which was static before, can now be dynamically adjusted by altering the magnetic flux Φ across the SQUID loop. This flux-tunability afforded by the DC SQUID, provides an essential tool for the precise control of quantum states and interactions.

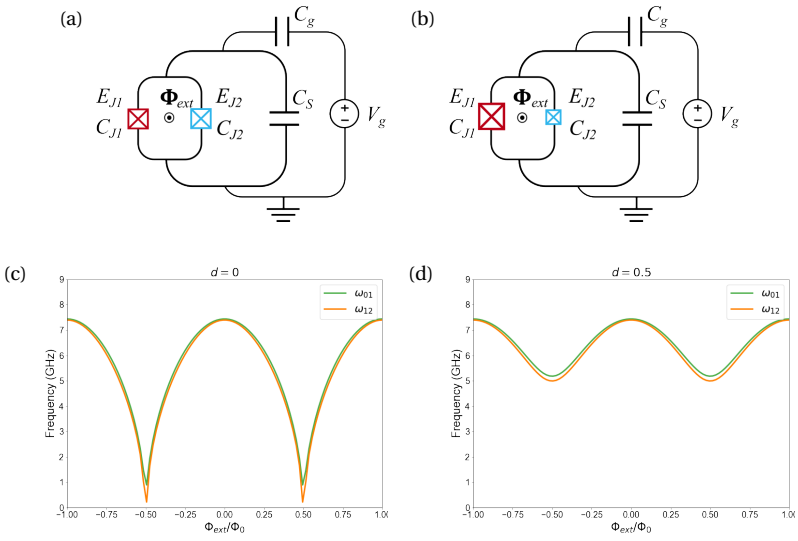

Figure 2.4: The schematic of tunable transmon and corresponding qubit transition frequencies for the three lowest energy states as a function of external magnetic flux Φ_{ext} in units of Φ_0. (*a*) A symmetric DC SQUID. (*b*) An asymmetric DC SQUID, with junction asymmetry $d = 0.5$. (*c*) The transition frequencies for a transmon qubit with the symmetric SQUID, parameters: $E_{j\Sigma}/2\pi = 40GHz$, $E_C/2\pi = 0.18GHz$. (*d*) The transition frequencies for a transmon qubit with the asymmetric SQUID, parameters: $E_{j\Sigma}/2\pi = 40GHz$, $E_C/2\pi = 0.18GHz$, $d = 0.5$. The transition frequency were obtained using the Scqubits package [24].

Combining DC SQUID into transmon qubits not only enhances the control of individual qubits but is also highly advantageous for multi-qubit circuits. This is because it allows selective participation of qubit interactions to circumvent the frequency collisions, unwanted interactions and mitigate the crosstalk, which benefits the scaling up of quantum processors. On the other hand, the ability to dynamically tune the qubit frequency also facilitates operations like two-qubit gates[40] and fast qubit reset.

Building on our understanding of DC SQUID and their impact on transmon qubits, we will now distinguish between symmetric and asymmetric DC SQUID, shown in Figs. 2.4a and 2.4b. Despite being a subtle difference, it significantly influences the functionality within quantum circuits, affecting tunability and noise susceptibility.

The slope of the qubit spectrum $\partial\omega/\partial(\frac{\Phi}{\Phi_0})$ shows the qubit sensitivity to flux noise. From Fig. 2.4c we can find when the two Josephson junctions are identical, the sensitivity is normally not zero unless at $\Phi/\Phi_0 = \pm 0.5$ where the slope is almost zero. But mean-

while, the transmon frequency is tuned down to near zero, which is too low for operating qubits with microwave pulses. For comparison, in Fig. 2.4d we plot the transition frequencies of tunable transmon qubits with an asymmetric DC SQUID. At $\Phi/\Phi_0 = \pm 0.5$, the slope $\partial\omega/\partial(\frac{\Phi}{\Phi_0})$ is still close to zero, but the qubit frequency has been improved meaning that standard microwave pulses can be used for the qubit control. However, the precise fabrication of the asymmetric DC SQUID with target parameters remains difficult, restricting their application.

Despite the design intricacies and distinct benefits of both symmetric and asymmetric tunable transmon qubits, one must note a common limitation: the anharmonicity, which is not significantly enhanced in these configurations.

2.3. FLUX QUBIT

Now we turn to another significant direction in the landscape of quantum circuit design: the flux qubits[41]. Instead of encoding quantum information in superconducting charge excitations as in charge qubits, flux qubits use the direction of persistent currents in a superconducting loop to define their quantum states[41]. These states, corresponding to the two lowest energy states, represent the two-level quantum system of the qubit, shown in Fig. 2.5a.

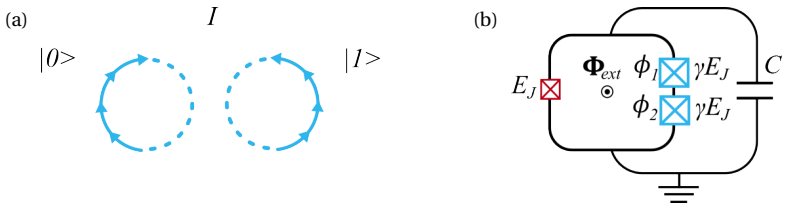

Figure 2.5: (*a*) The flux qubit system has two eigenstates $|0\rangle$ and $|1\rangle$ with opposite circulating persistent current. (b) Flux qubit circuit.

Similar to tunable transmon qubits, flux qubits also use SQUID loop in their design, where the loop is interrupted by three small-capacitance Josephson junctions, the Josephson energy in one of which is E_J, while the other two have equal Josephson energy γE_J, see Fig. 2.5b, and γ is the ratio of the E_J of large and small junctions. The potential energy profile is modified by an additional third junction in comparison to the transmon qubit with a SQUID. By using the quasi-1D approximation in $\gamma > 1$, the Hamiltonian can be approximated as[42]:

$$H \approx 4E_C N^2 - E_J \cos(\phi + \phi_e) - 2\gamma E_J \cos(\phi/2) \tag{2.25}$$

The parameters are similar to those of the DC SQUID, with an external flux of $\phi_e = 2\pi\Phi_{ext}/\Phi_0$ and $\phi = (\phi_1 + \phi_2)/2$ for two currents in the same direction.

The configuration of a flux qubit with a ratio $\gamma > 2$, yielding a single well potential, see Figs. 2.6a and 2.6c, which shares some similarities with the transmon qubit, both of

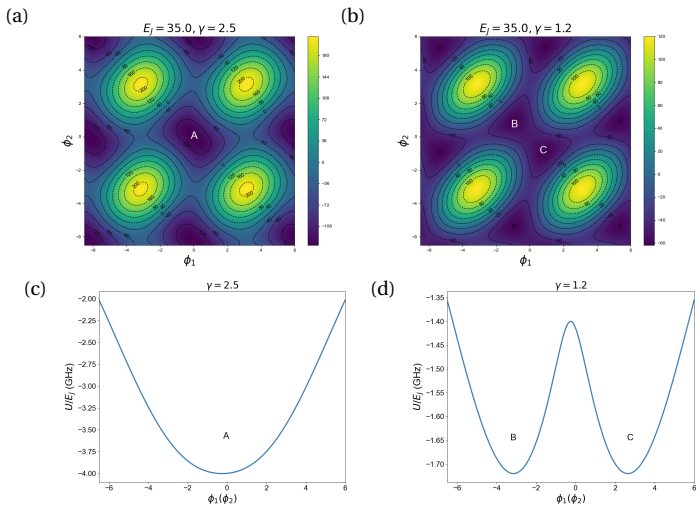

Figure 2.6: (*a*) and (*b*) are the contour plots for effective potential of the flux qubit in (ϕ_1, ϕ_2) plane for two different γ and under external magnetic flux $\Phi_{ext} = 0.5\Phi_0$. (*c*) and (*d*) represent the potential energy as a function of $\phi_1(\phi_2)$. The potential in (*c*) is at the point *A* for $\gamma = 2.5$, while the potential in (*d*) is drawn along the line connecting the points *B* and *C* for $\gamma = 1.2$. The potential energy was obtained using the Scqubits package [24].

which have a small anharmonicity. By reducing the ratio to $1 < \gamma < 2$[34], the change of the potential landscape from a single well to a double well structure can be achieved, shown in Figs. 2.6b and 2.6d. This crucial transformation brings a significant advantage: the ability to work with well-separated energy states.

In the double well regime, the lowest energy states of the system are primarily located in the two lowest potential wells. This structure effectively creates a two-level system, where transitions between the two lowest energy states are less likely to induce transitions to higher energy states due to the increased anharmonicity. Flux qubits encode quantum information differently from charge qubits and are therefore more resilient to charge noise. They are however more sensitive to flux noise due to their dependence on the magnetic flux through the loop.

2.3.1. FLUXONIUM

Based on the concept of flux qubits, we introduce fluxonium qubits, which, like flux qubits, encode quantum information in the flux of a superconducting loop. Unlike flux qubits, fluxonium qubits[4] include a key added element: superinductor, which allows them to reconcile the strengths of both charge and flux qubits. Structurally, the circuit of fluxonium qubits consists of a linear superinductance composed of an array of $N (N \approx 100)$ identical Josephson junctions, and a small Josephson junction shunted by a capacitance[43], as shown in Fig. 2.7.

For flux qubits, there are three Josephson junctions, so the last term in Eq. (2.25) is

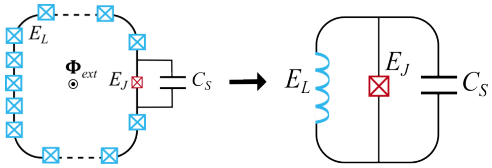

Figure 2.7: Circuit diagram of fluxonium qubit.

$-2\gamma E_J \cos(\phi/2)$, but the number of JJ array in fluxonium qubits can reach $N \approx 100$. In this case, using the same approximation, the Hamiltonian can be described as [42]:

$$H \approx 4E_C N^2 - E_J \cos(\phi + \phi_e) - N\gamma E_J \cos(\phi/N) \tag{2.26}$$

Since large JJ arrays can be regarded as the superinductor, the last term in Eq. (2.26) can be presented using inductive energy $E_L = (\gamma/N)E_J$. Eq. (2.26) can be rewritten as [42]:

$$H \approx 4E_C N^2 - E_J \cos(\phi + \phi_e) + \frac{1}{2}E_L \phi^2 \tag{2.27}$$

where the above parameters need to satisfy: $E_L \ll E_J$ and $1 \lesssim E_J/E_C \lesssim 10$, the quantity ϕ_e is the external magnetic flux[43], which plays a significant role in determining the properties of fluxonium qubit. When $\phi_e = 0$, the energy spectrum and the transition frequencies are similar to those of the transmon qubit, see Fig. 2.8a.

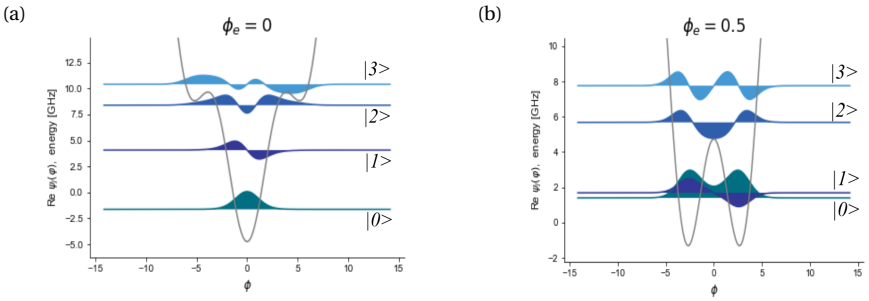

Figure 2.8: Potential energy structure is seen by the change of flux ϕ and the lowest four energy levels spectrum of the fluxonium qubit circuit, see Fig. 2.7, for two values of external flux ϕ_e. The potential energy were obtained using the Scqubits package [24].

However, when operating the qubit near the "sweet spot" ($\phi_e = 0.5$), the potential energy of fluxonium qubits have a double-well shape, as shown in Fig. 2.8b, leads to the two lowest eigenstates are primarily located in the two potential wells. This means that the energy difference between their ground and first excited states is substantially different from that between the first and second excited states. Such an energy level configuration represents the fluxonium qubit can exhibit a high anharmonicity energy spectrum when $\phi_e = 0.5$, which is beneficial for quantum computing as it allows for selective addressing of individual transition control.

3

TRANSMON AS TUNABLE COUPLER FOR TWO FLUXONIUM QUBITS

In this third chapter, we focus on the theoretical part of FXTFX device. In Section 3.1, we introduce the fundamentals of coupling between qubits, with emphasis on various methods and system designs that facilitate qubit interactions. Next, Section 3.2 explores the quantization of the circuit, details the energy interactions within the quantum system and addresses the coupling strength between the qubits. Finally, Section 3.3 gives the exploration into two-qubit gate, and offers a discussion on ZZ interaction.

3.1. INTRODUCTION

Several types of coupling schemes have been investigated[44–47], and our focus will predominantly be on capacitive coupling. In the subsequent sections of this chapter, we will delve into the details of the Hamiltonian for a capacitively coupled quantum system, then use it to form two-qubit gates.

3.1.1. CAPACITIVE COUPLING BETWEEN TWO QUBITS

Fig. 3.1a shows two qubits with direct capacitive coupling. The general form of the Hamiltonian for the coupled system can be written :

$$H = H_1 + H_2 + H_{int} \tag{3.1}$$

where H_1 and H_2 represent the Hamiltonian of the individual qubits, and H_{int} is the interaction Hamiltonian due to the capacitive coupling, which couples two quantum systems variables. The interaction is mediated by a coupling capacitor placed between the voltage nodes of the two superconducting circuits, which can be described by the

term[42]:

$$H_{int} = C_g V_1 V_2 \tag{3.2}$$

Here, V_1 and V_2 represent the voltage operators of the corresponding voltage nodes being connected, while C_g stands for the coupling capacitance. The coupling strength is directly related to the capacitance value C_g, thus adjusting C_g allows us to tune the interaction strength.

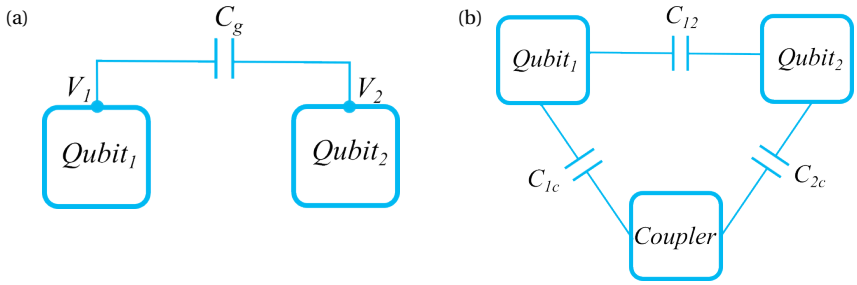

Figure 3.1: Schematic of the quantum system. (a) Direct capacitive coupling. (b) Capacitive coupling via coupler.

While as can be seen from Fig. 3.1a, the structure of direct capacitive coupling has apparent simplicity, it has some challenges when considering the development of large-scale quantum computers. The main drawback is that it leads to a phenomenon known as "frequency crowding". In a quantum system with multiple qubits, each qubit owns a unique frequency to avoid crosstalk. Hence, when designing large-scale quantum computers, one needs strategies to address the frequency crowding issue.

3.1.2. TUNABLE COUPLER

Addressing the challenges mentioned above, researchers turned their attention to a more sophisticated construct in quantum circuit design, tunable coupler, a novel introduction that offers a promising solution to thesis constraints. Tunable couplers, in essence, serve as controllable intermediaries between two qubits, see Fig. 3.1b. Multiple devices can perform this role, such as qubits[48–52], resonators[53, 54], and other objects[55, 56].

Compared with Eq. (3.1), the Hamiltonian of a quantum system incorporating a tunable coupler acquires an additional term:

$$H = H_1 + H_2 + H_c + H_{int} \tag{3.3}$$

H_1 and H_2 are the Hamiltonian of the individual qubits, as described in Eq. (3.1), and H_c is the Hamiltonian of the coupler. H_{int} now indicates the strength of the qubits interacting with the coupler and with each other.

Several studies have investigated the design of suitable tunable couplers for quantum circuits. For instance, using a single transmon qubit as a tunable coupler has been

proposed by researchers in [48, 57, 58]. However, this approach exists a correlated energy shift due to the residual ZZ coupling, which remains an undesired interaction. To mitigate this problem, a double-transmon coupler has been investigated as a potential solution [59]. Despite the advancements in transmon-based couplers, alternative designs utilizing different types of qubits have also been explored. Fluxonium qubits, due to their lower transition frequency and superior coherence properties, have emerged as promising candidates. Notably, Weiss et al. discussed the implementation of two fluxonium qubits interconnected via a flux-tunable coupler [60]. Similarly, the design of a fluxonium qubit as a coupler for two fluxonium qubits has also been proposed [50].

3.1.3. FLUXONIUM-TRANSMON-FLUXONIUM TUNABLE COUPLER SYSTEM

In this thesis, I aspire to integrate the benefits of both the transmon and fluxonium qubits by creating a unique circuit configuration where a tunable transmon qubit functions as a tunable coupler for fluxonium qubits, as illustrated in Fig. 3.2, and C_{ij} are the mutual capacitance between element i and element j.

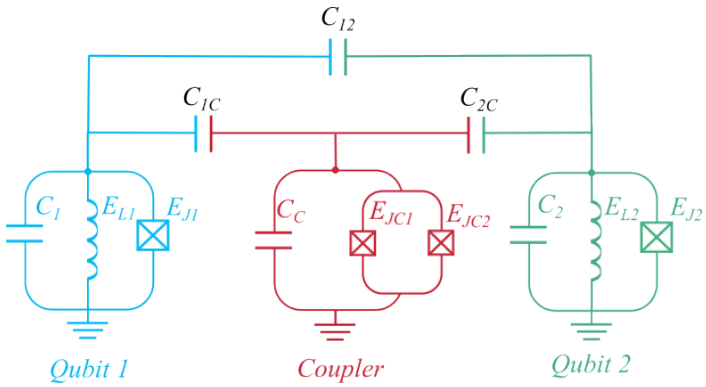

Figure 3.2: Circuit diagram of the implemented superconducting circuit, consisting of fluxonium qubit 1 (blue), fluxonium qubit 2 (green) and capacitively coupled to a tunable-transmon coupler (red).

In our quantum circuit design, the operating frequency of the tunable transmon qubit is inherently higher than that of the fluxonium qubits. This distinct frequency difference not only contributes to reducing potential frequency crowding issues but also aids in mitigating crosstalk. Besides, the tunable transmon qubit exhibits excellent tunability characteristics, which enables the construction of multi-qubit devices for large-scale quantum circuits.

3.2. QUANTIZATION OF THE CIRCUIT

In this section, I implement the aforementioned Fluxonium-Transmon-Fluxonium (FXTFX) system, delving into the mathematical details behind the quantization of our proposed circuit. Furthermore, I provide an estimation of the coupling strength among

the three qubits constituting our system.

3.2.1. DERIVATION OF THE HAMILTONIAN

Initially, we contemplate the general case of two fluxonium qubits coupled via a tunable coupler as illustrated in Fig. 3.3a. In this system, the two fluxonium qubits, denoted as Q_1 and Q_2, couple to each other with a coupling strength g_{12}, and each qubit couples to the tunable coupler with a coupling strength represented as g_{ic}, where $i \in \{1,2\}$.

Based on the simple chip layout of the FXTFX system, as depicted in Fig. 3.3a, the corresponding lumped-element circuit diagram is shown in Fig. 3.3b. The tunable transmon consists of a SQUID shunted by a capacitor. Unlike the tunable transmon with a single pad, each fluxonium qubit is equipped with two pads - top and bottom, which are individually connected by a small Josephson junction and an inductor. The capacitance between the two pads is C_{itib}, and each pad has its own grounding capacitance ($m \in \{1t, 1b, 2t, 2b\}$).

In order to derive the coupling strengths within the FXTFX system, we must first obtain the Hamiltonian of circuit. The derivation commences with the energetic terms corresponding to the constituents of the quantum circuit. As indicated by Equation Eq. (2.1), the energy stored within a capacitor, defined by the node flux Φ, is $T = \frac{1}{2}C\dot{\Phi}^2$. When this capacitor bridges two distinct flux nodes ϕ_i and ϕ_j, the energy term adjusts to $T = \frac{1}{2}C_{ij}(\dot{\Phi}_i - \dot{\Phi}_j)^2$.

Additionally, the Josephson energy of the tunable transmon E_{jc} is elucidated in Eq. (2.24) [40].

$$E_{Jc} = E_{J\Sigma}\cos\left(\frac{\pi\Phi_{ext}}{\Phi_0}\right)\sqrt{1 + d^2\tan^2\left(\frac{\pi\Phi_{ext}}{\Phi_0}\right)} \tag{3.4}$$

Here, $E_{J\Sigma} = E_{J_{c,l}} + E_{J_{c,r}}$ signifies the sum of the Josephson energies, where $E_{J_{c,l}}$ and $E_{J_{c,r}}$ are the Josephson energies of the left and right junctions, respectively, in the tunable transmon circuit. The term $d = \frac{E_{J_{c,l}} - E_{J_{c,r}}}{E_{J_{c,l}} + E_{J_{c,r}}}$ represents the relative junction asymmetry. Φ_{ext} is the external magnetic flux through the loop of the tunable transmon circuit.

In Fig. 3.3b, we number nodes from $1t$ to $2b$ on the top and bottom pads of two fluxonium qubits and the node of the tunable coupler as c. Consequently, the Lagrangian ($\mathscr{L}$) of circuit is represented in terms of node flux Φ, can be formulated by combining

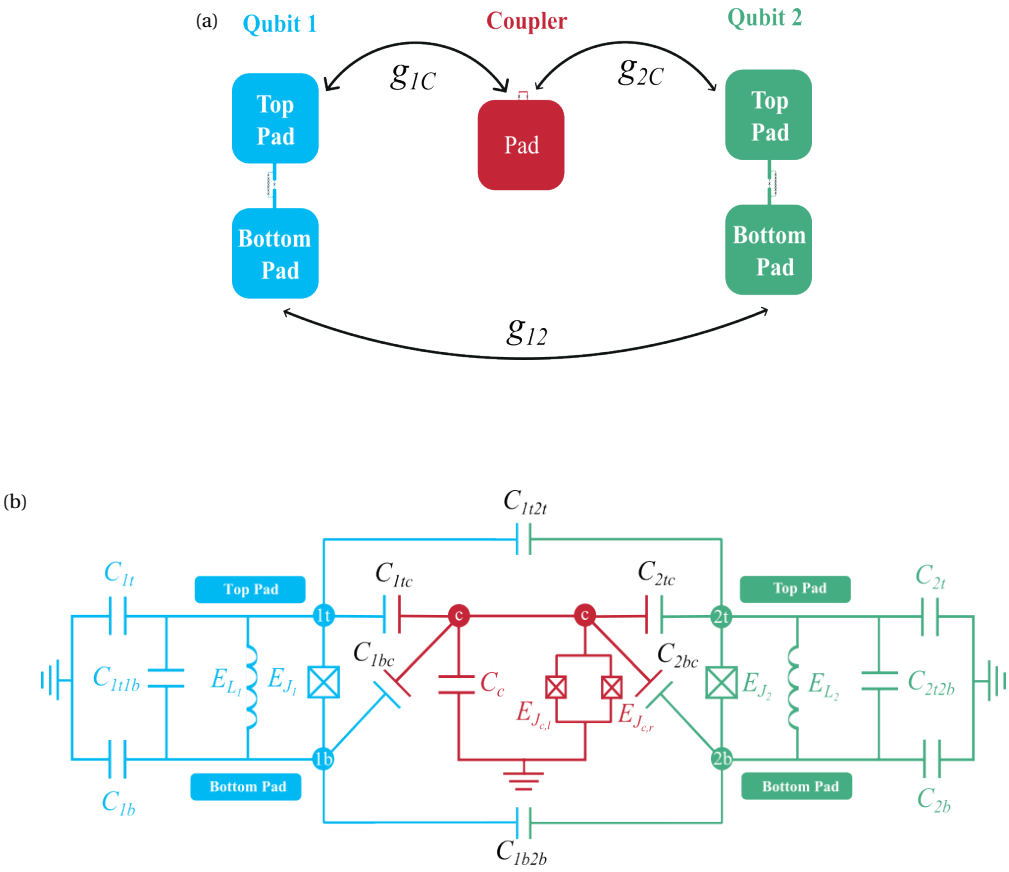

Figure 3.3: (a) A schematic of a tunable coupler (red) mediating the coupling between two fluxonium qubits (blue and green). The qubit-coupler coupling is described by g_{1c}, g_{2c}, and the direct qubit-qubit coupling is described by g_{12}. (b) The lumped-element circuit representation of the schematic in (a). And false colors (blue, red and green) are used to indicate the corresponding circuit components in (a). E_{Li} stands for the inductive energy, E_{Ji} indicates for the Josephson energy, C_i denotes for the capacitance of the pad with respect to the ground, C_{ij} are the mutual capacitance between node i and j.

the kinetic energy (T) and potential energy (U) terms for the complete quantum circuit:

$$
\begin{aligned}
T = \frac{1}{2}[&C_{1t}\dot{\Phi}_{1t}^2 + C_{1b}\dot{\Phi}_{1b}^2 + C_c\dot{\Phi}_c^2 + C_{2t}\dot{\Phi}_{2t}^2 + C_{2b}\dot{\Phi}_{2b}^2 \\
&+ C_{1t1b}(\dot{\Phi}_{1t} - \dot{\Phi}_{1b})^2 + C_{1tc}(\dot{\Phi}_{1t} - \dot{\Phi}_c)^2 + C_{1t2t}(\dot{\Phi}_{1t} - \dot{\Phi}_{2t})^2 + C_{1t2b}(\dot{\Phi}_{1t} - \dot{\Phi}_{2b})^2 \\
&+ C_{1b1t}(\dot{\Phi}_{1b} - \dot{\Phi}_{1t})^2 + C_{1bc}(\dot{\Phi}_{1b} - \dot{\Phi}_c)^2 + C_{1b2t}(\dot{\Phi}_{1b} - \dot{\Phi}_{2t})^2 + C_{1b2b}(\dot{\Phi}_{1b} - \dot{\Phi}_{2b})^2 \\
&+ C_{c1t}(\dot{\Phi}_c - \dot{\Phi}_{1t})^2 + C_{c1b}(\dot{\Phi}_c - \dot{\Phi}_{1b})^2 + C_{c2t}(\dot{\Phi}_c - \dot{\Phi}_{2t})^2 + C_{c2b}(\dot{\Phi}_c - \dot{\Phi}_{2b})^2 \\
&+ C_{2t1t}(\dot{\Phi}_{2t} - \dot{\Phi}_{1t})^2 C_{2t1b}(\dot{\Phi}_{2t} - \dot{\Phi}_{1b})^2 + C_{2tc}(\dot{\Phi}_{2t} - \dot{\Phi}_c)^2 + C_{2t2b}(\dot{\Phi}_{2t} - \dot{\Phi}_{2b})^2 \\
&+ C_{2b1t}(\dot{\Phi}_{2b} - \dot{\Phi}_{1t})^2 C_{2b1b}(\dot{\Phi}_{2b} - \dot{\Phi}_{1b})^2 + C_{2bc}(\dot{\Phi}_{2b} - \dot{\Phi}_c)^2 + C_{2b2t}(\dot{\Phi}_{2b} - \dot{\Phi}_{2t})^2]
\end{aligned}
$$

$$
\begin{aligned}
U = &- E_{J1}\cos\left(2\pi\frac{\Phi_{1t} - \Phi_{1b}}{\Phi_0} + 2\pi\frac{\Phi_{e1}}{\Phi_0}\right) - E_{J2}\cos\left(2\pi\frac{\Phi_{2t} - \Phi_{2b}}{\Phi_0} + 2\pi\frac{\Phi_{e2}}{\Phi_0}\right) - E_{Jc}\cos\left(2\pi\frac{\Phi_c}{\Phi_0} + 2\pi\frac{\Phi_{ec}}{\Phi_0}\right) \\
&+ \frac{E_{L1}}{2}(2\pi\frac{\Phi_{1t} - \Phi_{1b}}{\Phi_0})^2 + \frac{E_{L2}}{2}(2\pi\frac{\Phi_{2t} - \Phi_{2b}}{\Phi_0})^2
\end{aligned}
$$

$$
\mathscr{L} = T - U \tag{3.5}
$$

where

$$
\Phi_0 c = \tan^{-1}[d\tan\frac{\Phi_{ec}}{2}] \tag{3.6}
$$

In the equation above, T and U denote the kinetic and potential energies of the quantum system respectively. $\Phi_0 = \frac{h}{2e}$ is the magnetic flux quantum and Φ_i corresponds to the node flux associated with node $i \in \{1t, 1b, 2t, 2b, c\}$. Φ_{ek}, $(k = 1, 2, c)$ is the external magnetic flux through the loops.

For ease of mathematical manipulation, the kinetic energy term can be rewritten in matrix form $T = \frac{1}{2}\dot{\vec{\Phi}}^T\mathbf{C}\dot{\vec{\Phi}}$. Here, $\dot{\vec{\Phi}}$ represents the vector $[\dot{\Phi}_{1t}, \dot{\Phi}_{1b}, \dot{\Phi}_c, \dot{\Phi}_{2t}, \dot{\Phi}_{2b}]$, and $\mathbf{C}$ is a 5×5 capacitance matrix expressed as follows:

$$
\mathbf{C} = \begin{bmatrix}
\mathbb{C}_{11} & -C_{1t1b} & -C_{1tc} & -C_{1t2t} & -C_{1t2b} \\
-C_{1t1b} & \mathbb{C}_{22} & -C_{1bc} & -C_{1b2t} & -C_{1b2b} \\
-C_{1tc} & -C_{1bc} & \mathbb{C}_{33} & -C_{c2t} & -C_{c2b} \\
-C_{1t2t} & -C_{1b2t} & -C_{c2t} & \mathbb{C}_{44} & -C_{2t2b} \\
-C_{1t2b} & -C_{2t2b} & -C_{c2b} & -C_{2t2b} & \mathbb{C}_{55}
\end{bmatrix} \tag{3.7}
$$

The diagonal elements of this matrix are ascribed by:

$$\begin{aligned}
\mathbb{C}_{11} &= C_{1t} + C_{1t1b} + C_{1tc} + C_{1t2t} + C_{1t2b} \\
\mathbb{C}_{22} &= C_{1b} + C_{1b1t} + C_{1bc} + C_{1b2t} + C_{1b2b} \\
\mathbb{C}_{33} &= C_c + C_{c1t} + C_{c1b} + C_{c2t} + C_{c2b} \\
\mathbb{C}_{44} &= C_{2t} + C_{2t1t} + C_{2t1b} + C_{2tc} + C_{2t2b} \\
\mathbb{C}_{55} &= C_{2b} + C_{2b1t} + C_{2b1b} + C_{2bc} + C_{2b2t}
\end{aligned} \tag{3.8}$$

Given the relatively large distance separating the two fluxonium qubits, the capacitance between them is quite minimal, essentially nearing zero. Thus, the capacitive interaction between two fluxonium qubits can be neglected, and we can approximate:

$$C_{1t2t} = C_{1t2b} = C_{1b2t} = C_{1b2b} \approx 0 \tag{3.9}$$

With this simplification, the capacitance matrix can be rewritten into:

$$\mathbf{C} = \begin{bmatrix}
\mathbb{C}_{11} & -C_{1t1b} & -C_{1tc} & 0 & 0 \\
-C_{1t1b} & \mathbb{C}_{22} & -C_{1bc} & 0 & 0 \\
-C_{1tc} & -C_{1bc} & \mathbb{C}_{33} & -C_{c2t} & -C_{c2b} \\
0 & 0 & -C_{c2t} & \mathbb{C}_{44} & -C_{2t2b} \\
0 & 0 & -C_{c2b} & -C_{2t2b} & \mathbb{C}_{55}
\end{bmatrix} \tag{3.10}$$

The updated diagonal elements can now be presented by:

$$\begin{aligned}
\mathbb{C}_{11} &= C_{1t} + C_{1t1b} + C_{1tc} \\
\mathbb{C}_{22} &= C_{1b} + C_{1b1t} + C_{1bc} \\
\mathbb{C}_{33} &= C_c + C_{c1t} + C_{c1b} + C_{c2t} + C_{c2b} \\
\mathbb{C}_{44} &= C_{2t} + C_{2tc} + C_{2t2b} \\
\mathbb{C}_{55} &= C_{2b} + C_{2bc} + C_{2b2t}
\end{aligned} \tag{3.11}$$

With the Lagrangian of the circuit, we define the generalized momenta q_i, which is the node charges, corresponding to the node flux Φ_i:

$$q_i = \frac{\partial \mathscr{L}}{\partial \dot{\Phi}_i} \tag{3.12}$$

Building upon the Lagrangian previously derived in Eq. (3.5), Eq. (3.12) can be rewritten in vector form as $\vec{q} = \mathbb{C}\dot{\vec{\Phi}}$. Here, $\vec{q} = [q_{1t}, q_{1b}, q_c, q_{2t}, q_{2b}]^T$.

Then apply the Lagrangian to Hamiltonian conversion, the Hamiltonian representation below:

$$\hat{H} = \vec{q} \cdot \dot{\vec{\Phi}} - \mathscr{L} = \frac{1}{2} \vec{q}^T \mathbf{C}^{-1} \vec{q} + U \tag{3.13}$$

However, the Hamiltonian derived in 3.13 is based on the top and bottom pads of each fluxonium qubit, which can be called pad basis. This means that the Hamiltonian can only be obtained for the coupling strength from pad to pad, and from pad to the coupler. However, this pad basis perspective is insufficient for a comprehensive understanding of the system dynamics, particularly when interested in inter-qubit and qubit-coupler interactions. Thus, it's necessary to convert to the qubit basis representation of the Hamiltonian.

To make this transition from pad basis to qubit basis, it is essential to transform the standard flux variables into a novel set of flux variables based on sum and difference coordinates. This transformation isolates and emphasizes the critical dynamics that define the fluxonium qubit behavior and its interaction with another fluxonium qubit or coupler. In order to effect this transformation, transformation matrix $\mathbf{M}$ is introduced, defined as:

$$\mathbf{M} = \begin{bmatrix} 1 & -1 & 0 & 0 & 0 \\ 1 & 1 & 0 & 0 & 0 \\ 0 & 0 & 1 & 0 & 0 \\ 0 & 0 & 0 & 1 & -1 \\ 0 & 0 & 0 & 1 & 1 \end{bmatrix} \tag{3.14}$$

By applying this transformation matrix, the new flux variables are driven $\widetilde{\Phi}$ as shown in Eq. (3.15)

$$\widetilde{\Phi} = \mathbf{M}\vec{\Phi} \tag{3.15}$$

$$\widetilde{\Phi} = \begin{bmatrix} \Phi_{1t} - \Phi_{1b} \\ \Phi_{1t} + \Phi_{1b} \\ \Phi_c \\ \Phi_{2t} - \Phi_{2b} \\ \Phi_{2t} + \Phi_{2b} \end{bmatrix} = \begin{bmatrix} \Phi_1 \\ \Phi_{1\Sigma} \\ \Phi_c \\ \Phi_2 \\ \Phi_{2\Sigma} \end{bmatrix} \tag{3.16}$$

From Eq. (3.15), the initial flux vector and its transpose in terms of the new flux variables are rewritten as follows:

$$\vec{\Phi} = \mathbf{M}^{-1}\widetilde{\Phi}, \qquad \vec{\Phi}^T = \widetilde{\Phi}^T(\mathbf{M}^{-1})^T \tag{3.17}$$

Details of the $\mathbf{M}^{-1}$ and $(\mathbf{M}^{-1})^T$ matrixes are given in Appendix A.

As a direct consequence of this transformation, the kinetic energy term, originally formulated in terms of the pad basis, can now be expressed in the qubit basis:

$$T = \frac{1}{2}\dot{\vec{\Phi}}^T\mathbf{C}\dot{\vec{\Phi}} = \frac{1}{2}\dot{\widetilde{\Phi}}^T(\mathbf{M}^{-1})^T\mathbf{C}\mathbf{M}^{-1}\dot{\widetilde{\Phi}} = \frac{1}{2}\dot{\widetilde{\Phi}}^T\widetilde{\mathbf{C}}\dot{\widetilde{\Phi}} \tag{3.18}$$

Here, $\widetilde{\mathbf{C}}$ denotes the transformed capacitance matrix in the qubit basis.

Subsequently, we define the new canonically conjugate momenta $\widetilde{q}$, which corresponds to the variables introduced in Eq. (3.16), as follows:

$$\widetilde{q}_i = \frac{\partial \mathscr{L}}{\partial \dot{\widetilde{\Phi}}_i} \tag{3.19}$$

The momenta vector then becomes $\widetilde{q} = [q_1, q_{1\Sigma}, q_c, q_t, q_{2\Sigma}]^T$.

Using canonical quantization, we could obtain the Hamiltonian:

$$\hat{H} = \frac{1}{2}\vec{q}^T\mathbf{C}^{-1}\vec{q} + U = \frac{1}{2}\widetilde{q}^T\widetilde{\mathbf{C}}^{-1}\widetilde{q} + U \tag{3.20}$$

with $\mathbf{C}^{-1}$ being the new inverse capacitance matrix. This implies that by employing matrix $\mathbf{M}$ to perform a variable transformation, we have effectively transitioned from a pad basis perspective to a qubit basis description of the Hamiltonian.

3.2.2. COUPLING STRENGTH

In the previous subsection, we discussed the Hamiltonian of the FXTFX system from the perspective of the qubit basis. In this subsection, we will calculate the coupling strength between the qubits using the Hamiltonian given by Eq. (3.20).

Let's start by revisiting the general expression of the Hamiltonian for the FXTFX system. We can express it as follows:

$$\begin{aligned} \hat{H} &= \sum_i \hat{H}_i + \sum_{i\neq j} \hat{H}_{ij}, \quad \{i,j\} \in \{1,2,c\} \\ &= \hat{H}_1 + \hat{H}_2 + \hat{H}_c + \hat{H}_{12} + \hat{H}_{1c} + \hat{H}_{2c} \end{aligned} \tag{3.21}$$

Here, $\hat{H}_i$ donates the Hamiltonian of the individual fluxonium qubits and tunable coupler, while $\hat{H}_{ij}$ indicates the interaction between two fluxonium qubits and each with tunable coupler.

It's important to note that in the fluxonium qubit, the qubit basis is determined only by the coordinates Φ_1 and Φ_2. This is because the difference in flux between the top and bottom pads of a fluxonium qubit corresponds to the variable primarily used to encode information. The sum flux variables $\Phi_{1\Sigma}$ and $\Phi_{2\Sigma}$ do not significantly contribute to the dynamics of interest in our FXTFX system. This is due to the fact that the sum variables typically represent uniform net charges distributed on the pads, therefore the sum mode can be considered as "free particles" in the system [51] and can be neglected when writing down the Hamiltonian.

Taking this into account, we can derive the following Hamiltonian expressions for

the individual fluxonium qubits and the coupler from Eq. (3.5):

$$\begin{aligned}
\hat{H}_1 &= -E_{J1}\cos\left(2\pi\frac{\Phi_1}{\Phi_0}+2\pi\frac{\Phi_{e1}}{\Phi_0}\right)+\frac{E_{L1}}{2}\Phi_1^2+\frac{1}{2}\mathbf{C}^{-1}[1,1]q_1^2\\
\hat{H}_2 &= -E_{J2}\cos\left(2\pi\frac{\Phi_2}{\Phi_0}+2\pi\frac{\Phi_{e2}}{\Phi_0}\right)+\frac{E_{L2}}{2}\Phi_2^2+\frac{1}{2}\mathbf{C}^{-1}[4,4]q_2^2\\
\hat{H}_c &= -E_{Jc}\cos\left(2\pi\frac{\Phi_c}{\Phi_0}+2\pi\frac{\Phi_{ec}}{\Phi_0}\right)+\frac{1}{2}\mathbf{C}^{-1}[3,3]q_c^2
\end{aligned} \tag{3.22}$$

We can introduce $E_C=\frac{e^2}{2C}$, $\phi=\frac{2\pi\Phi}{\phi_0}$ and $\hat{n}=\frac{q}{2e}$, which is the Cooper-pair number operator. So Eq. (3.22) can be rewritten as:

$$\begin{aligned}
\hat{H}_1 &= -E_{J1}\cos\left(\phi_1+\phi_{e1}\right)+\frac{E_{L1}}{2}\phi_1^2+4E_{C1}\hat{n}_1^2\\
\hat{H}_2 &= -E_{J2}\cos\left(\phi_2+\phi_{e2}\right)+\frac{E_{L2}}{2}\phi_2^2+4E_{C2}\hat{n}_2^2\\
\hat{H}_c &= -E_{Jc}\cos\left(\phi_c+\phi_{ec}\right)+4E_{Cc}\hat{n}_1^2
\end{aligned} \tag{3.23}$$

Here,

$$E_{C1}=e^2\mathbf{C}^{-1}[1,1],\quad E_{C2}=e^2\mathbf{C}^{-1}[4,4],\quad E_{Cc}=e^2\mathbf{C}^{-1}[3,3] \tag{3.24}$$

Next, the interaction Hamiltonian can be obtained from Eq. (3.20):

$$\begin{aligned}
\hat{H}_{1c} &= \frac{1}{2}\widetilde{\mathbf{C}}^{-1}[1,3]q_1q_c+\frac{1}{2}\widetilde{\mathbf{C}}^{-1}[3,1]q_1q_c=4e^2\widetilde{\mathbf{C}}^{-1}[1,3]\hat{n}_1\hat{n}_c\\
\hat{H}_{2c} &= \frac{1}{2}\widetilde{\mathbf{C}}^{-1}[4,3]q_2q_c+\frac{1}{2}\widetilde{\mathbf{C}}^{-1}[3,4]q_2q_c=4e^2\widetilde{\mathbf{C}}^{-1}[3,4]\hat{n}_2\hat{n}_c\\
\hat{H}_{12} &= \frac{1}{2}\widetilde{\mathbf{C}}^{-1}[1,4]q_1q_4+\frac{1}{2}\widetilde{\mathbf{C}}^{-1}[4,1]q_1q_4=4e^2\widetilde{\mathbf{C}}^{-1}[1,4]\hat{n}_1\hat{n}_2
\end{aligned} \tag{3.25}$$

And the inverse capacitance matrix is symmetric, we have $\widetilde{\mathbf{C}}^{-1}[i,j]=\widetilde{\mathbf{C}}^{-1}[j,i]$.

We can also express the interaction Hamiltonian as follows:

$$\hat{H}_{1c}=\hbar g_{1c}\hat{n}_1\hat{n}_c,\quad \hat{H}_{2c}=\hbar g_{2c}\hat{n}_2\hat{n}_c,\quad \hat{H}_{12}=\hbar g_{12}\hat{n}_1\hat{n}_2 \tag{3.26}$$

By comparing these expressions, we can find that:

$$g_{1c}=\frac{4e^2\widetilde{\mathbf{C}}^{-1}[1,3]}{\hbar},\quad g_{2c}=\frac{4e^2\widetilde{\mathbf{C}}^{-1}[3,4]}{\hbar},\quad g_{12}=\frac{4e^2\widetilde{\mathbf{C}}^{-1}[1,4]}{\hbar} \tag{3.27}$$

Here, g_{1c},g_{2c} is the qubit-coupler coupling, and the direct qubit-qubit coupling for two fluxonium qubits is described by g_{12}. The formula of $\widetilde{\mathbf{C}}^{-1}[1,3]$, $\widetilde{\mathbf{C}}^{-1}[3,4]$ and $\widetilde{\mathbf{C}}^{-1}[1,4]$ are illustrated in Appendix A.

The derived coupling strengths set the stage for a deeper analysis of the dynamics of the FXTFX system, which will be helpful for device design and optimization.

3.3. QUBIT GATES IN SUPERCONDUCTING CIRCUIT

In this section, we describe how two-qubit gates work in the FXTFX system.

3.3.1. TWO-QUBIT GATES

Two-qubit gates are fundamental quantum gates that act on two qubits simultaneously. These gates introduce entanglement between qubits, which is a crucial resource for quantum computing. Some well-known two-qubit gates are: Controlled-Not (CNOT) gate, Controlled-Z (CZ) Gate and iSWAP Gate. They are all the control gates, one qubit is chosen as the control qubit and the unitary operator will be applied for another qubit, also called the target qubit based on the state of control qubit. In this thesis, we will discuss how to implement the CZ gate with the FXTFX device.

The unitary operator of the CZ gate can be written as the 4×4 matrix.

$$\mathbf{U_{CZ}} = \begin{bmatrix} 1 & 0 & 0 & 0 \\ 0 & 1 & 0 & 0 \\ 0 & 0 & 1 & 0 \\ 0 & 0 & 0 & -1 \end{bmatrix} \tag{3.28}$$

When the state of control qubit is $|1\rangle$, the target qubit will be rotated by π phase ($e^{i\pi} = -1$).

There are several methods to implement the CZ gate, and we will use the Rabi Oscillation approach. This method uses resonant interactions to drive Rabi oscillations between the $|11\rangle$ state and a higher energy state like $|12\rangle$ or $|21\rangle$. By driving a π-pulse, the system can be excited from $|11\rangle$ to $|12\rangle$ (or $|21\rangle$) and then brought back to $|11\rangle$, picking up a phase of π in the process. If this phase is properly controlled, a CZ gate can be realized[7, 8].

3.3.2. ZZ INTERACTION

ZZ interaction originates from level repulsion between the energy level with both qubits in the first excited state and some non-computational energy levels[61], which can lead to unwanted phase shifts, thus affecting the fidelity of quantum gates.

ZZ interaction is quantified by the parameter ζ, defined as:

$$\zeta = \frac{E_{101} - E_{001} - E_{100} + E_{000}}{\hbar} \tag{3.29}$$

Here, E_m represents the eigenenergy corresponding to the eigenstate $|m\rangle$. The quantum state of the system are represented by $|nmk\rangle$, where n, m, and k correspond to the eigenstates of fluxonium 1, the coupler (tmon), and fluxonium 2, respectively.

In the field of fast two-qubit gates, higher coupling strength is generally desirable. However, higher coupling strengths usually have the negative effect of increased ζ.

To understand this behavior quantitatively, we can expand ζ into its nth-order perturbation contributions, $\zeta^{(n)}$, using the corresponding nth-order corrections $E_m^{(n)}$, ($n \in \{2,3,4\}$), to the eigenenergies of $|m\rangle$:

$$\zeta^{(n)} = \frac{E_{101}^{(n)} - E_{001}^{(n)} - E_{100}^{(n)} + E_{000}^{(n)}}{\hbar} \tag{3.30}$$

And the perturbed result for ZZ interaction ζ can be defined as:

$$\zeta = \zeta^{(2)} + \zeta^{(3)} + \zeta^{(4)} \tag{3.31}$$

The n-order energy shift to the state $|m\rangle$ is:

$$E_m^{(2)} = \sum_{j \neq m} \frac{|V_{mj}|^2}{E_{mj}^{(0)}} \tag{3.32}$$

$$E_m^{(3)} = \sum_{j,k \neq m} \frac{V_{mj} V_{jk} V_{km}}{E_{mj}^{(0)} E_{mk}^{(0)}} \tag{3.33}$$

$$E_m^{(4)} = \sum_{j,k,l \neq m} \frac{V_{mj} V_{jk} V_{kl} V_{lm}}{E_{mj}^{(0)} E_{mk}^{(0)} E_{ml}^{(0)}} - \sum_{j,k \neq m} \frac{|V_{mj}|^2 |V_{mk}|^2}{(E_{mj}^{(0)})^2 E_{mk}^{(0)}} \tag{3.34}$$

where $V_{mj} = \langle m|\hat{H}_{int}|j\rangle$ represents the matrix element of the interaction Hamiltonian between states $|m\rangle$ and $|j\rangle$. And $E_{mj}^{(0)} = E_m^{(0)} - E_j^{(0)}$, $E_m^{(0)}$ and $E_j^{(0)}$ are the unperturbed energies of these states.

3.3.3. DRIVING HAMILTONIAN

The driving Hamiltonian used is given by [62]:

$$\hat{H}_d = \varepsilon(t) \times \hat{n} \tag{3.35}$$

Here, $\varepsilon(t)$ is the control pulse and n is the charge operator. $\varepsilon(t)$ is depicted as [42, 63]:

$$\varepsilon(t) = \varepsilon_I(t) \sin(\omega_d t) + \varepsilon_Q(t) \cos(\omega_d t) \tag{3.36}$$

where $\varepsilon_I(t)$ and $\varepsilon_Q(t)$ represent time-dependent amplitudes of the in-phase and out-of-phase quadrature components of the pulse, respectively, and ω_d is the drive frequency.

$$\varepsilon_I(t) = \frac{\Omega}{2}\left[1 - \cos\left(\frac{2\pi t}{\tau_g}\right)\right] \tag{3.37}$$

Choosing the envelope to make sure the ramping is smooth, Ω is drive amplitude and τ_g is the total duration of the gate operation.

The latter term in Eq. (3.36) is introduced by the derivative removal by adiabatic gate (DRAG) technique to mitigate the leakage. In this case, the first order DRAG is proportional to the first derivative of the in-phase pulse that can be written as[63]:

$$\varepsilon_Q(t) = \lambda \frac{\dot{\varepsilon}_I(t)}{\eta} \tag{3.38}$$

where λ is a scaling parameter and η is the anharmonicity. Adjusting λ can effectively modify the control pulse to mitigate the unwanted transitions (leakage) from the computational subspace to higher energy levels. When $\lambda = 0$, this means that no DRAG modulation is applied.

4

DEVICE DESIGN AND SIMULATION

In this chapter, our primary focus is well-designed and simulated FXTFX chip. Section 4.1 describes the intricate design of fluxonium qubit. The design and subsequent simulation of resonators are explored in Sections 4.2 and 4.3, respectively. Moving forward, Section 4.4 delves into the design methodologies and simulation techniques for tunable transmon qubits. The FXTFX device, which is the core of our discussion, is elaborated in Section 4.5, where we illuminate the approaches for determining and enhancing the coupling strength. Concluding the chapter, Section 4.6 is wholly dedicated to the detailed simulations of the FXTFX device, ensuring a comprehensive understanding of its functionality.

4.1. FLUXONIUM QUBIT DESIGN

In our superconducting device, the fluxonium qubits play a pivotal role as the primary data-carrying entities, storing quantum information that will be eventually read out at the conclusion of a quantum computation. The specific design we utilize for the fluxonium qubit, as proposed by F. Yilmaz [64], is presented in Fig. 4.1. At the heart of the fluxonium qubit are its essential components, each fulfilling a specific role:

- **Capacitor**: Represented by the two yellow pads in Figure 4.1.
- **Josephson Junction**: Positioned centrally between the two capacitor pads, It is a non-linear element.
- **Super-inductance**: Located on the left side of the Josephson junction, this element is composed of an array of 100 Josephson junctions. It aids in enhancing protection against charge noise.
- **Flux Biasing Line**: The green line in the figure is inductive coupled to the qubit, which provides a means to apply magnetic flux to the fluxonium loop. This capability allows for adjusting the energy levels of qubit.

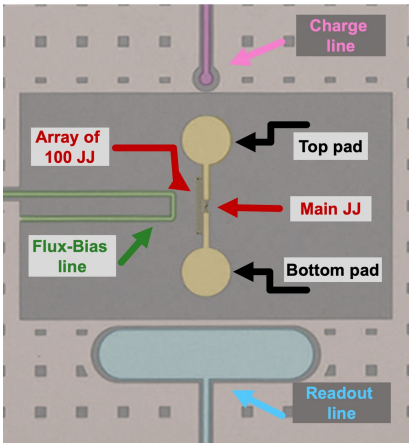

Figure 4.1: Fabricated Chip layout of a fluxonium qubit with false coloring.

- **Charge Line**: The pink line in the figure is capacitively coupled to the qubit capacitor. It is used to apply microwave pulses, which can induce state transitions in the qubit, facilitating precise qubit control.
- **Readout Resonator**: The blue pad, along with the twisted line, is capacitively coupled to both the fluxonium qubit and the feedline.

4.2. RESONATOR DESIGN AND PROPERTIES

In quantum circuits, resonators play a critical role in interactions between the qubits and the surrounding environment. Various types of resonators are available for use in quantum circuits, each with unique properties and applications. In this thesis, we choose to work with coplanar waveguide (CPW) resonators.

4.2.1. GEOMETRY AND MATERIAL SELECTION

The planar geometry of a CPW is depicted in Fig. 4.2, consisting of a central conductor surrounded by a pair of return conductors, with planes separated by a gap, and the entire structure positioned on a substrate. The characteristic impedance of the CPW is a crucial parameter and is typically set to a standard value of 50 Ω. This choice represents a balanced comes [65]. Furthermore, adhering to this standard impedance ensures that the CPW resonator will be compatible with the majority of electronic devices, which are often designed to operate at 50 Ω. However, due to imperfections in our PCB fabrication, we are faced with a characteristic impedance of 42 Ω. In response to this deviation, we chose to set the impedance of the launch pad (Z_0) and the CPW resonator (Z_r) to about 45 Ω. This decision is aimed at reducing impedance mismatch at both the PCB and the electronic device interfaces. By choosing an intermediate value, we aim to balance the impedance across these interfaces, thus minimizing insertion losses.

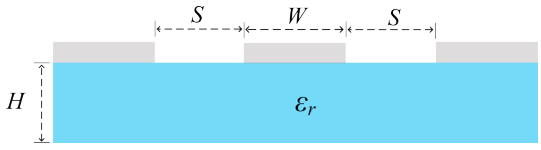

Figure 4.2: Cross section of CPW resonator design. Central conductor and lateral ground plan (gray) on top of the substrate(blue). Parameters are discussed in the main text.

In order to achieve this, the design of our CPW line requires a careful selection of materials and geometrical parameters. In our chip, the substrate is made of silicon and the superconducting material of conductor is Niobium Titanium Nitride (NbTiN). Utilizing a CPW calculator[66], the characteristic impedance Z_0 and effective dielectric constant ϵ_{eff} for a CPW can be obtained respectively. The used parameters in our design are listed in Table 4.1.

Parameter	Symbol	Value
Center strip width	W	15 μm
Gap width	S	5.909 μm
Substrate thickness	H	525± 10 μm
Dielectric constant	ϵ_r	11.5 (low temperature)[67]
Effective permittivity	ϵ_{eff}	6.249
Characteristic impedance	Z_r	45.046 Ω

Table 4.1: The parameters of CPW

4.2.2. FREQUENCY AND LENGTH OPTIMIZATION

The next step is to define the frequency of the resonator, denoted by f_0, which is derived from the wavelength of the signal and its phase velocity. This relationship can be expressed as $f_0 = \frac{v}{\lambda}$. v is the phase velocity of the microwave signal, and λ represents the wavelength. They can be further related to the physical properties of the CPW line[68]:

$$v = \frac{c}{\epsilon_{\text{eff}}}, \quad \lambda = 2l \tag{4.1}$$

Where c is the velocity of light in vacuum, ϵ_{eff} is the effective permittivity of the CPW line, and l is the length of the resonator. Thus, the resonator frequency f_0 is given as:

$$f_0 = \frac{c}{\sqrt{\epsilon_{\text{eff}}}} \frac{1}{2l} \tag{4.2}$$

It is clear from Eq. (4.2) that the frequency f_0 is inversely proportional to the length of the CPW, given a fixed ϵ_{eff}. Generally, superconducting resonators for quantum circuits are designed to operate within a microwave frequency range, typically from 4 to 8 GHz[69],

and this frequency range is well supported by readily available commercial microwave equipment.

The selection of distinct frequencies for each resonator is not an arbitrary choice. By ensuring a clear separation in the resonance frequencies, we can control and probe individual resonators without cross-interference. This isolation is essential for precise qubit manipulation and measurement. Furthermore, distinct frequencies mitigate the risk of crosstalk, where signals intended for one resonator inadvertently affect another.

4.2.3. DETERMINING COUPLING QUALITY FACTOR AND DECAY RATE

There are two main CPW resonator designs. The quarter-wavelength: In this design, one end of the resonator is shorted, while the other remains open. The other is the half-wavelength resonator: For this configuration, both ends of the resonator are either open or shorted. This is the design we have opted for. As depicted in Fig. 4.3a, the half-wavelength resonator is structured with a CPW line. One side features a coupler with an open end, while the opposite side terminates in an open end with a readout pad. This configuration can be further explored in Figs. 4.3b and 4.3c.

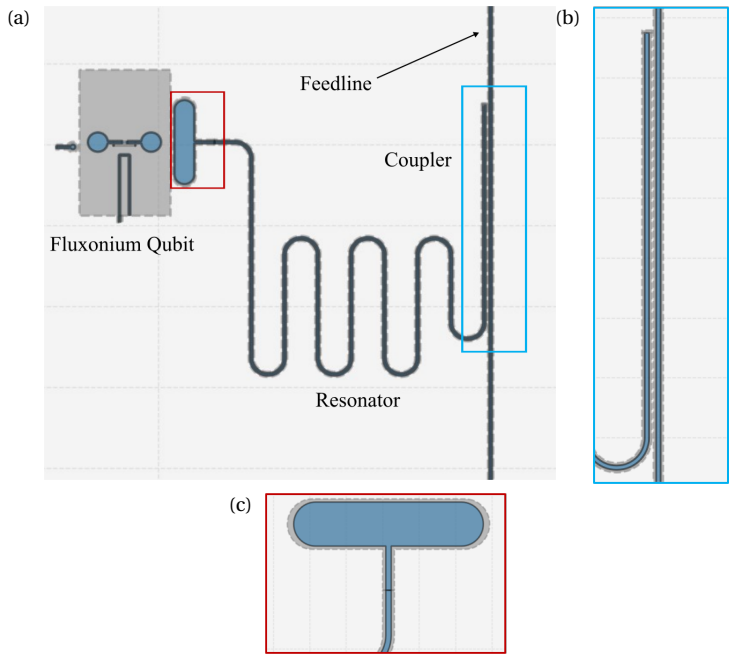

Figure 4.3: (a) Image of a single fluxonium qubit, displaying the half-wavelength CPW microwave resonator. The resonator capacitive couples to a feedline at one extremity and to a fluxonium qubit at the other. (b) Zoom in on the capacitive coupler between the resonator and the feedline. (c) Magnified view of the fluxonium qubit readout pad, which connects to one end of the resonator.

Then we will introduce another critical parameter in the design of resonators is the coupling quality factor, denoted as Q_c. This factor signifies the degree to which the res-

onator couples to the feedline. Both the length of the coupler, as shown in Fig. 4.3b, and the distance between the through feedline and the part of the resonator running parallel with it, determines the coupling factor Q_c. The coupling quality factor Q_c of half-wave resonator can be expressed as[70]:

$$Q_c = \frac{\pi}{\omega_r^2 Z_0 Z_r C_k^2} \tag{4.3}$$

In the above equation, ω_r represents the angular frequency of the resonator and is related to the resonance frequency f_0 by $\omega_r = 2\pi f_0$. Z_0 and Z_r are the characteristic impedance of the feedline and CPW line. C_k, referred to as the coupling capacitance, defines the capacitive coupling between the resonator and the feedline.

From Q_c, we can derive the resonator decay rate, κ, which quantifies the rate at which energy is dissipated from the resonator. A higher decay rate can mean faster energy loss, and based on Taryn Stefanski's simulation results, it is necessary to keep $\kappa/2\pi$ around 5 MHz [63]. The relationship between the decay rate and the quality factor is given by[71]:

$$\kappa = \frac{f_0}{Q_c} \tag{4.4}$$

4.3. RESONATOR SIMULATIONS

With a comprehensive understanding of the resonator design and parameters, it's imperative to evaluate its performance through simulation. For this purpose, the electromagnetic (EM) simulation software ANSYS-HFSS is used, which allows obtaining the frequency of resonator. Coupling capacitance C_k between the resonator and the feedline can be obtained using ANSYS-Q3D. In addition, it is able to calculate the coupling quality (Q_c) and the decay rate (κ).

4.3.1. DESIGN AND LAYOUT

Superconducting device is usually read by sending a radiofrequency (RF) pulse through a feedline, which is coupled to a resonator and the resonator is coupled to a qubit. However, the resonators need to be modeled with Qiskit-Metal, before simulations can be performed. We integrated four FXTFX devices into the chip, which bolsters redundancy, and it is vital in reducing vulnerabilities related to fabrication inconsistencies or defects.

To begin, I establish the initial design frequencies for the eight resonators in the circuit. These frequencies are tabulated as follows:

Resonator	1	2	4	5	7	8	10	11
Frequency(GHz)	6.8	7.2	7.6	8.0	6.3	6.0	5.7	5.2

Table 4.2: The frequencies of eight resonators

After determining these frequencies, I proceed to calculate the initial lengths for each resonator. This calculation is based on the formula previously introduced in Eq. (4.2). After the initial lengths are identified, I then lay out these resonators in the circuit, as illustrated in Fig. 4.4. All resonators are capacitively coupled to the same feedline, and obviously, each resonator has a different length.

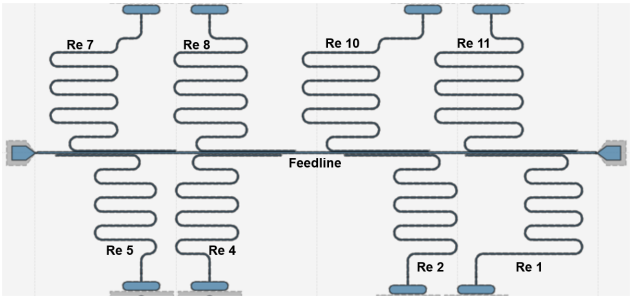

Figure 4.4: The bird view of the readout system. “Q 1” to “Q 11” indicate the locations of the eight fluxonium qubits. The feedline across through the full chip to make sure each resonator is coupled to it conventionally.

4.3.2. SIMULATION AND ANALYSIS

Once the resonator system has been constructed, it can be analyzed through an energy participation ratio (EPR) analysis to obtain its resonant frequency. The process begins with the creation and activation of an eigenmode design in Qiskit-Metal that I named "Res". This resonator is then rendered corresponding to the design in ANSYS-HFSS. Refer to Fig. 4.5a for the illustrative model. Following this, the convergence parameters and junction properties are set within the ANSYS-HFSS design. The subsequent step involves running the analysis. Electric field distribution of the eigenmode can be visualized in Fig. 4.5b. With this, the resonant frequencies are computed.

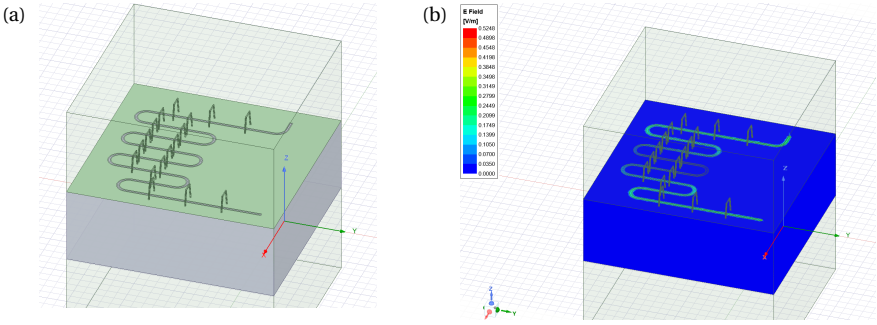

Figure 4.5: (a) The resonator is rendered corresponding to the "Res" design in ANSYS-HFSS. (b) Electric field distribution of the eigenmode for the same resonator.

It's essential to compare the simulation frequency outcomes with the values in Table 4.2. If discrepancy occurs, revisit the design and make necessary adjustments for the length of resonator according to the inverse relationship mentioned in Eq. (4.2), followed by re-simulation until the simulation result matches the initial design value. The method is also applied to the other resonators, and the individual frequencies of each resonator can be obtained, referred to the "bare frequency" in Table 4.3. Bare frequency denotes the resonator natural resonance frequency when it remains unaffected by any external interactions or influences.

4.3.3. EVALUATION OF DRESSED FREQUENCY

However, the resonator in the chip is coupled to the fluxonium qubit. The interaction can induce a shift in the resonator energy level, yielding a frequency, termed the "dressed frequency" that is different from the bare frequency. To address this phenomenon and quantify the dressed frequency, a joint simulation of the qubit and resonator is performed.

The dressed frequency simulations are performed using the quantum part of the EPR analysis. Creating an analysis object for the combined qubit and resonator, called "Qubit-Res", as depicted in Fig. 4.6a.

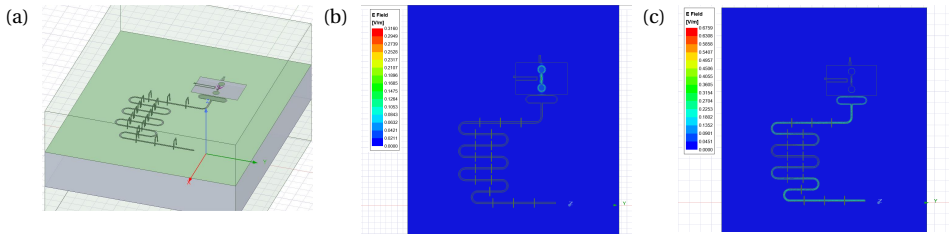

Figure 4.6: (a) The "Qubit-Res" schematic as visualized in ANSYS-HFSS. (b) Electric field distribution of qubit mode. (c) Electric field distribution of resonator mode.

A fundamental distinction lies in the eigenmode number: while a singular eigenmode suffices for the bare frequency, the dressed frequency needs to look for 2 eigenmodes. One with stronger fields on the fluxonium, called qubit mode and the other with stronger fields on the resonator (resonator mode). The electric field distributions for two modes are shown in Figs. 4.6b and 4.6c, respectively. Applying this methodology to the other resonators, all dressed frequencies are given, as tabulated in Table 4.3.

Resonator	1	2	4	5	7	8	10	11
Initial Design Frequency(GHz)	6.8	7.2	7.6	8.0	6.3	6.0	5.7	5.2
Bare Frequency(GHz)	6.813	7.216	7.615	8.034	6.363	5.968	5.699	5.195
Dressed Frequency(GHz)	6.109	6.474	6.765	7.087	5.751	5.437	5.186	4.778

Table 4.3: Comparison of initial design, bare, and dressed frequencies across the eight resonators.

A straight phenomenon from Table 4.3 is that the dressed frequency consistently lies below its bare frequency for all resonators. This can be attributed to the connection between the large readout pad of fluxonium qubit and resonator in Fig. 4.3c, which contributes additional capacitance. Recalling the inverse relationship between frequency and capacitance, it is evident that an increase in the capacitance decreases the resonator frequency, resulting in the dressed frequency being lower than the bare frequency.

4.3.4. EVALUATION OF COUPLING CAPACITANCE AND DECAY RATE

With the frequencies determined, our next step is to ascertain the decay rate, denoted as κ. To achieve this, it's imperative to first understand the coupling capacitance C_k between the resonators and the feedline. For this purpose, the Maxwell capacitance matrix in Lumped Oscillator Model (LOM) analysis is employed.

After selecting Resonators 10 and setting up the analysis in ANSYS-Q3D, the Maxwell capacitance matrix[72] can be extracted, see Fig. 4.7.

	g_wb	trace_cavity10	trace_TL
g_wb	3244.07410	-1735.59339	-1288.93441
trace_cavity10	-1735.59339	1774.99038	-37.71266
trace_TL	-1288.93441	-37.71266	1327.98780

Figure 4.7: The capacitance matrix for resonator 10 with the feedline. The unit of capacitance is fF.

Within the capacitance matrix:

- `"trace_cavity01"` symbolizes resonator 10.
- `"trace_TL"` denotes the transmission line.
- The intersecting squares' values in the rows and columns signify the coupling capacitance between associated elements.
- The matrix is symmetric, and the main diagonal values reflect the algebraic sum of their respective row elements.

From Fig. 4.7, the coupling capacitance between resonator and the feedline is 37.71 fF. Using the dressed frequency and coupling capacitance, the coupling quality factor Q_c and decay rate κ both can be driven. The following table describes coupling capacitance, Q_c and κ for each resonator.

A detailed derivation of the coupling quality factor and decay rate is given in the Appendix C.

Resonator	1	2	4	5	7	8	10	11
$f_0(\omega_r/2\pi)$ (GHz)	6.109	6.474	6.765	7.087	5.751	5.437	5.186	4.778
Coupling Capacitance(fF)	28.87	26.78	24.58	23.35	31.49	34.36	37.71	42.66
Q_c	1262.78	1306.21	1420.11	1434.28	1198.60	1128.85	1029.74	948.94
$\kappa/2\pi$ (MHz)	4.83	4.95	4.76	4.94	4.79	4.81	5.03	5.02

Table 4.4: Summary of resonator parameters. The table includes the dressed frequencies (f_0), coupling capacitances C_k, coupling quality factors (Q_c), and decay rates (κ) for each resonator.

4.4. TUNABLE TRANSMON QUBIT DESIGN AND SIMULATION

The tunable transmon serves as the pivotal component within our circuit, functioning as the coupler interfacing with two fluxonium qubits.

Traditionally, the most prevalent tunable transmon is the Xmon[73]. This design derives its name from the characteristic 'cross' structure it forms, constructed by intersecting two superconducting coplanar waveguide lines, exemplified in Fig. 4.8a. However, from Eq. (A.2) we find that the difference between the top pad to the coupler capacitance C_{1tc}/C_{c2t} and the bottom pad to the coupler capacitance C_{1bc}/C_{c2b} contributes significantly to the coupling strength, which can use $C_{1bc}-C_{1tc}$ or $C_{c2b}-C_{c2t}$ to express. Thus, Xmon exhibits a week coupling strength when coupled with two fluxonium qubits.

To address this limitation, we propose a novel design: Tmon, visually resembling a Half-Xmon qubit, see Fig. 4.8b, which was originally implemented in Qiskit-Metal by Figen. It's worth noting that, contrary to the simplistic structure in figure, the Josephson junction actually contains a SQUID loop that interfaces with the flux line, allowing for qubit frequency tuning.

(a)

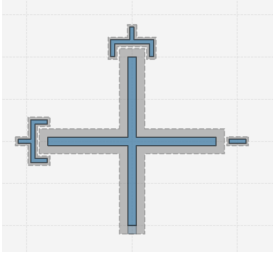

(b)

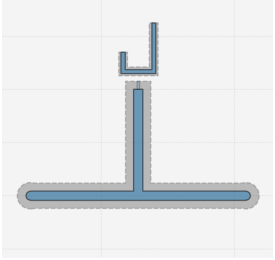

(c)

	flux_bias_line_Q1	ground_main_plane	tmon_Q1
flux_bias_line_Q1	62.23778	-61.28064	-0.70706
ground_main_plane	-61.28064	309.61469	-179.65994
tmon_Q1	-0.70706	-179.65994	183.28317

Figure 4.8: (a) Xmon qubit design [39]. (b) Proposed tmon qubit design. (c) Capacitance matrix of the Tmon qubit. The unit of capacitance is fF.

With the structure of the tunable transmon, the next step is to refine the qubit pa-

rameters by obtaining the Maxwell capacitance matrix through LOM analysis, Fig. 4.8c shown here. Since the tmon qubit is grounded, the total capacitance C_Σ can be expressed directly in terms of the capacitance between tmon and ground, as 179 fF. $E_c/2\pi = 107$ MHz can be derived according to the relationship between capacitance and charging energy in Eq. (2.17). The Josephson energy E_{Jc} can be modulated by adjusting the surface area of the Josephson junction when the other parameters are fixed [74].

4.5. FXTFX DEVICE DESIGN

Previous section focuses on the design of the tmon qubit. In this section, I integrate the tmon qubit with fluxonium qubits to create the full FXTFX device. Based on the simulation results, I then make appropriate design adjustments.

4.5.1. DETERMINING THE COUPLING STRENGTH

The first step in the analysis is to determine the coupling strengths g_{12}, g_{1c}, and g_{2c} of the FXTFX device, which can be computed using Eq. (3.27) and Eq. (A.2). To calculate these values, the layout of the FXTFX device without charge lines, flux lines and resonators was developed and simulated, as shown in Fig. 4.9.

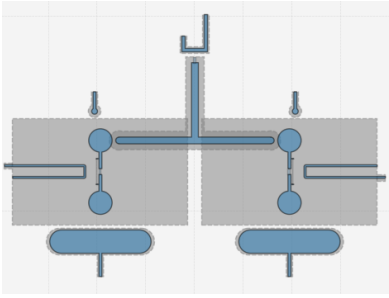

Figure 4.9: Chip layout of the FXTFX device.

The coupling capacitances between different elements of the FXTFX device were calculated, and the results are as follows:

$$\begin{aligned}
&C_{1t1b} = C_{1b1t} = 3.167\text{fF}, \quad C_{2t2b} = C_{2b2t} = 3.169\text{fF} \\
&C_{1tc} = 6.251\text{fF}, \quad C_{c2t} = 6.251\text{fF}, \quad C_{1bc} = 1.789\text{fF}, \quad C_{c2b} = 1.787\text{fF} \\
&C_{1t} = 22.182\text{fF}, \quad C_{2t} = 22.175\text{fF}, \quad C_{1b} = 20.713\text{fF}, \quad C_{2b} = 20.718\text{fF} \\
&C_c = 118.740\text{fF}, \quad C_{11} = 31.593\text{fF}, \quad C_{22} = 25.658\text{fF} \\
&C_{33} = 13.480\text{fF}, \quad C_{44} = 31.593\text{fF}, \quad C_{11} = 25.658\text{fF}
\end{aligned} \tag{4.5}$$

By entering these capacitances in Eq. (A.2), the values of $\mathbf{C}^{-1}[1,3]$, $\mathbf{C}^{-1}[3,4]$, and $\mathbf{C}^{-1}[1,4]$ can be calculated. Based on the relationship between the inverse matrix elements in

Eq. (3.27) and the coupling strength, the coupling strength between qubits can be derived, summarized in Table 4.5.

	$g_{1c}/2\pi$ (MHz)	$g_{2c}/2\pi$ (MHz)	$g_{12}/2\pi$ (MHz)
Coupling Strength	127.24	127.36	13.74

Table 4.5: The coupling strengths of the FXTFX device

The coupling strengths are crucial as they define the timescale for qubit entanglement and two-qubit gates. Essentially, the stronger coupling between qubits makes the gate faster and is the basis of efficient quantum computing.

4.5.2. DESIGN ADJUSTMENTS FOR ENHANCED COUPLING

In an effort to enhance the overall performance of quantum operations, I revisited the design of the tmon qubits with a specific focus on optimizing their coupling strengths.

DESIGN MODIFICATIONS

Two main design modifications were considered for enhancing the coupling strengths:

- Increasing the surface area of the ends of the tmon qubits, which I will refer to as the 'Round Ends' design (Fig. 4.10a).
- Modifying the geometry of the Tmon ends to adopt a 'claw' shape, which I will refer to as the 'Claw Ends' design (Fig. 4.10b).

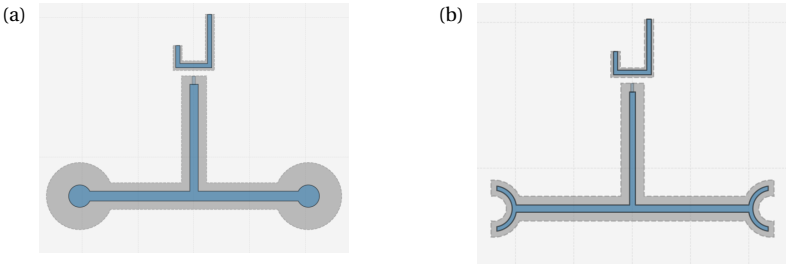

Figure 4.10: (a) Tmon design with rounded ends. (b) Tmon design with claw-shaped ends.

After redesigning, the new tmon qubit is integrated into the existing fluxonium qubit systems. The new coupling strengths are obtained, as tabulated below in Table 4.6.

As observed, the claw-shaped end design shows noticeably higher coupling strengths compared to the Round Ends design. Importantly, the Round Ends design limits me to adjustments based solely on the radius and distance between the tmon and fluxonium.

	$g_{1c}/2\pi$ (MHz)	$g_{2c}/2\pi$ (MHz)	$g_{12}/2\pi$ (MHz)
Coupling Strength(Round Ends)	186.84	186.77	29.23
Coupling Strength(Claw Ends)	368.03	368.41	132.71

Table 4.6: The coupling strengths of the FXTFX device with redesigned tmon qubits.

In contrast, the Claw Ends design comes with several adjustable parameters. This flexibility allows to fine-tune the coupling strengths to specific requirements, and is particularly beneficial for high-performance quantum operations.

FINE-TUNING THE CLAW DESIGN

The Claw Ends design allows for various parameters to be fine-tuned, such as the distance between the claw of the tmon and the fluxonium pad, the length of the claw itself, and the inter-fluxonium distance. Here, I demonstrate five different settings for the FXTFX device, visualized in Figs. 4.11a to 4.11e.

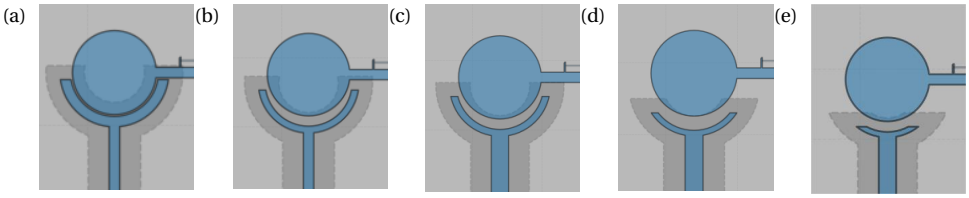

Figure 4.11: Diagram of different configurations for five FXTFX devices. (a) Structure I. (b) Structure II. (c) Structure III. (d) Structure IV. (e) Structure V.

	Structure I	Structure II	Structure III	Structure IV	Structure V
$g_{1c}/2\pi(g_{2c}/2\pi)$ (MHz)	395.56	322.82	299.60	226.56	191.910
$g_{12}/2\pi$ (MHz)	161.28	90.71	81.089	42.55	30.663

Table 4.7: The coupling strengths of the five FXTFX devices with different properties.

Coupling strengths for these five configurations are given in Table 4.7. The results confirm that the claw design provides a great degree of freedom in adjusting the strength of the coupling. Such flexibility not only allows for the optimization of quantum operations but also offers a pathway to customizing quantum devices for specific computational tasks.

The following simulations are based on Structure IV, as shown in Fig. 4.11d.

After completing the design of tmon, the layout of full chip design is illustrated in Fig. 4.12:

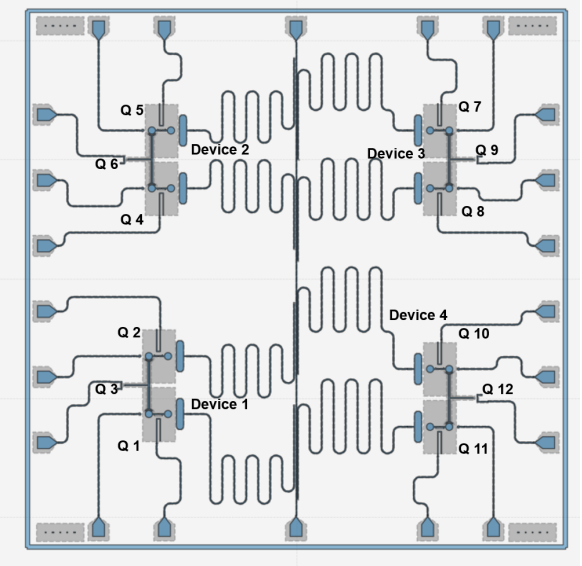

Figure 4.12: The layout of the full chip.

4.6. FXTFX DEVICE SIMULATION

In the previous section, we discussed how to determine the coupling strengths for various parameter configurations. Utilizing these strengths, we are able to derive the full Hamiltonian for the FXTFX system, thereby providing insights into its behavior and properties. In this section, we focus specifically on the simulation of CZ gate using tunable couplers in FXTFX devices.

4.6.1. DRIVE FREQUENCY OF CZ GATES

We begin our investigation of the CZ gate by performing energy spectroscopy on correlated energy state transitions. As previously discussed in Section 3.3.1, the CZ gate can be implemented by driving the $|11\rangle$ state to either the $|12\rangle$ or $|21\rangle$ state, and then reverting it back to $|11\rangle$.

In our FXTFX system, the transmon frequency significantly exceeds that of the fluxonium qubits. This hierarchy of frequencies results in the coupler mainly interacting with the higher energy states of the fluxonium qubits, thus enabling the performance of two-qubit operations without significantly affecting single-qubit gates.

We donate the quantum state of the system as $|nmk\rangle$, where n, m, and k represent the eigenstates of fluxonium 1, the coupler (tmon), and fluxonium 2, respectively. By using the similar approach in Section 3.3.1, the CZ gate can be achieved by deriving $|101\rangle$ state to $|102\rangle$ either $|201\rangle$ or $|111\rangle$ states.

ROLE OF DRIVE FREQUENCY

In implementing CZ gates using the Rabi oscillation technique, a crucial parameter to consider is the drive frequency. Rabi oscillations are inherently sensitive to the frequency of the applied microwave drive, as they determine transitions between specific quantum states.

For instance, transitioning from the $|101\rangle$ to $|201\rangle$ state requires a drive frequency that should be different from the one needed for transitioning from $|100\rangle$ to $|200\rangle$. In the absence of the interaction Hamiltonian $H_{int} = 0$, the transition frequencies obey the following relationship:

$$\omega_{101\to201} = \omega_{100\to200} = \omega_{1\to2}^{f1}, \qquad \omega_{101\to102} = \omega_{001\to002} = \omega_{1\to2}^{f2} \tag{4.6}$$

Introducing an interaction Hamiltonian into the system couples the individual qubits, leading to a more complex energy level structure as illustrated in Fig. 4.13.

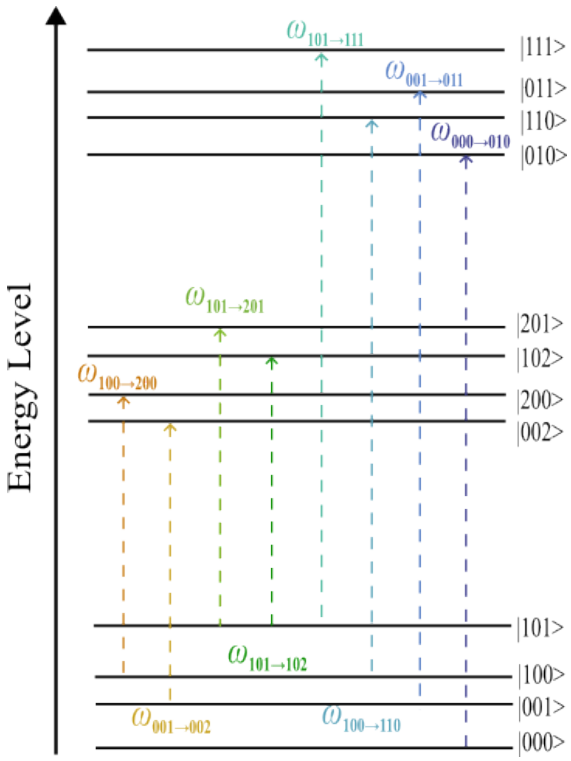

Figure 4.13: The energy level structure of the coupled system.

The interaction Hamiltonian, as given by Eq. (3.26), can be formulated as follows:

$$H_{int} = \hbar g_{1c} n_1 n_c + \hbar g_{2c} n_2 n_c + \hbar g_{12} n_1 n_2 \tag{4.7}$$

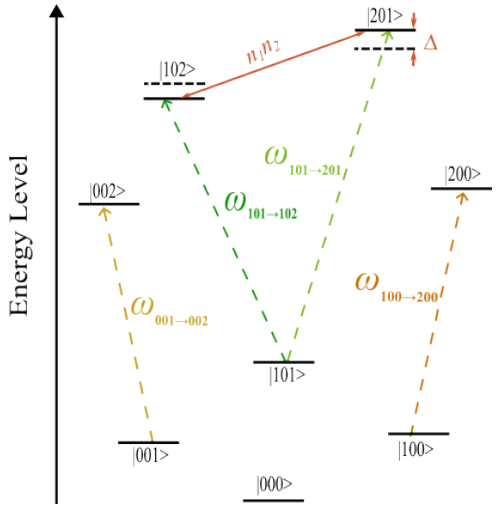

Figure 4.14: The energy level structure of the full system for FXTFX device.

Due to this energy repulsion, the degeneracy of transition frequencies will be boosted:

$$\omega_{101\to201} \neq \omega_{100\to200}, \qquad \omega_{101\to102} \neq \omega_{001\to002} \tag{4.8}$$

The parameter Δ in Fig. 4.14 indicates the frequency mismatch between the transitions $\omega_{101\to201}$ and $\omega_{100\to200}$ transitions. When Δ is sufficiently large, a targeted pulse can selectively transition the system from $|101\rangle$ to $|201\rangle$ state while preserving the closest transition $|100\rangle$ to $|200\rangle$ remains unexcited. This allows for the CZ gate to be implemented with individually addressable transitions, enhancing its robustness. The same principle can be extended to implement CZ gates for $|101\rangle \to |102\rangle$ and $|101\rangle \to |111\rangle$ transitions.

In fact, the gate time is characterized by Δ, in general, larger values of Δ lead to faster gate[7]. Consequently, optimizing Δ becomes a pivotal task. One strategy for increasing Δ involves carefully selecting Hamiltonian parameters for the fluxonium qubits and examining the resulting energy level separations.

DETERMINING THE OPTIMAL EXCITATION PATH FOR CZ GATE

In this section, I use the Scqubits package[24] to determine the most suitable excitation path for the implementation of CZ gate. The focus is primarily on assessing the frequency mismatches Δ across different devices.

One of the primary challenges in fabricating fluxonium qubits is achieving uniformity in the JJ array. Given the precision required in the fabrication process, there are often discrepancies in the E_J values between different fluxonium qubits within the same device. To investigate how these discrepancies influence the frequency mismatch within

		$E_C/2\pi$(GHz)	$E_L/2\pi$(GHz)	$E_J/2\pi$(GHz)
Device A/B/C	Fluxonium 1	1.005	0.816	4.75
	Coupler	0.18		40 (d=0)
Device A	Fluxonium 2	1.005	0.806	4.39
Device B	Fluxonium 2	1.005	0.806	4.55
Device C	Fluxonium 2	1.005	0.806	4.70
	$g_{12}/2\pi$(GHz)		$g_{1c}/2\pi(g_{2c}/2\pi)$(GHz)	
Device A/B/C	0.042		0.226	

Table 4.8: The Hamiltonian parameters for Device A, Device B and Device C. d is the junction asymmetry, with d = 0 indicating that the two Josephson junctions of the coupler (tmon) are identical.

the FXTFX system, I consider three different device configurations in Table 4.8, each characterized by varying E_J values for the second fluxonium qubit.

To assess the frequency mismatches (Δ) for different Hamiltonian parameters in the FXTFX system, an external flux sweep on the coupler ($\Phi_{ext,c}$) is performed for each device configuration. The results, as depicted in Figs. 4.15a and 4.15b, showcase the frequency mismatches Δ^{201} and Δ^{111} across Devices A, B, and C.

From Fig. 4.15a, it is observed that $\Delta^{201} = \omega_{101\to201} - \omega_{100\to200}$ holds the relationship: $\Delta_C^{201} > \Delta_B^{201} > \Delta_A^{201}$. The underlying reason for this ranking can be attributed to when both fluxonium qubits are in excited states, the larger similarity of the Hamiltonian parameters leads to a stronger repulsion between the $|102\rangle$ and $|201\rangle$ energy levels. Such an effect is observed as an increase in the Δ value, which is advantageous for enabling faster CZ gates.

While modifying the Hamiltonian parameters of fluxonium qubit affects Δ^{201}, it keeps Δ^{111} unchanged, as shown in Fig. 4.15b. The transition from $|101\rangle$ to $|111\rangle$ easily leads to a large Δ^{111} compared to the other two transitions. Only when the external flux of the coupler is between 0.38 and 0.4 can Δ^{201} reach above 0.1 GHz, and this requires a relatively high similarity between the Hamiltonian parameters for two fluxonium qubits. In contrast, for the transition from $|101\rangle$ to $|111\rangle$, a relatively high Δ^{111} is more easily attained by tuning $\Phi_{ext,c}/\Phi_0$ around 0.2 or 0.25.

Further simulations of the transition from $|101\rangle$ to $|111\rangle$ investigate the effect of varying the Josephson energy (E_J) of the tunable coupler on the frequency mismatch Δ^{111}. When varying the E_J of the transmon (35, 40, and 45 GHz), it is easy to realize Δ^{111} above 0.1 GHz by choosing a suitable $\Phi_{ext,c}$ as shown in Fig. 4.15c.

The simulations reveal that regardless of the specific E_J value, a smooth and substantial frequency mismatch can be obtained by fine-tuning $\Phi_{ext,c}$.

Therefore, I finally chose $|101\rangle$ to $|111\rangle$ transition for CZ gate in the following content.

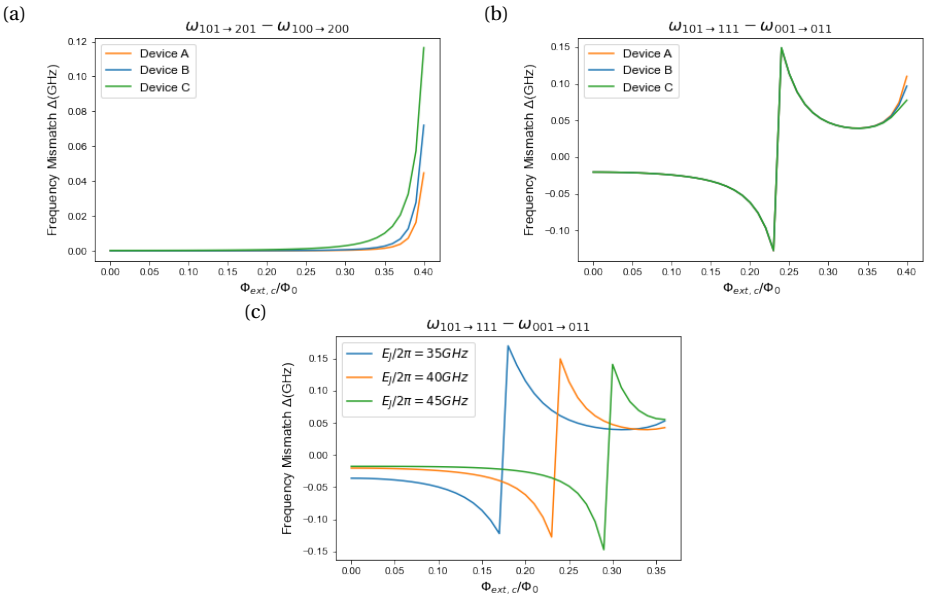

Figure 4.15: (a) The frequency mismatch $\omega_{101\to201} - \omega_{100\to200}$ for Devices A, B, and C. (b) The frequency mismatch $\omega_{101\to111} - \omega_{001\to011}$ for all Devices. (c) The frequency mismatch $\omega_{101\to111} - \omega_{001\to011}$ with different E_J for Device C.

FREQUENCY MISMATCH USING MEASURED FLUXONIUM QUBITS FOR CZ GATE

Having established the $|101\rangle$ to $|111\rangle$ transition as the foundation for the CZ gate implementation in the FXTFX system, the next step is to delve into the precise calculations that will guide the quantum gate operations.

Fluxonium qubits in Fig. 4.12 are measured, and the Hamiltonian parameters of fluxonium qubits 7 and 8 in Device 3 are listed in Table 4.9. Other parameters (coupler and coupling strengths) are still the designed values.

		$E_C/2\pi$(GHz)	$E_L/2\pi$(GHz)	$E_J/2\pi$(GHz)
Device 3	Fluxonium 7	0.858	0.835	3.732
	Fluxonium 8	0.864	0.827	3.815
	Coupler	0.18		40 (d=0)

	$g_{12}/2\pi$(GHz)	$g_{1c}/2\pi(g_{2c}/2\pi)$(GHz)
Device 3	0.042	0.226

Table 4.9: The Hamiltonian parameters for Device 3.

With these parameters as the foundation, Δ^{111} for Devices 3, as demonstrated in

Fig. 4.16, inform us about the optimal operating points for our system.

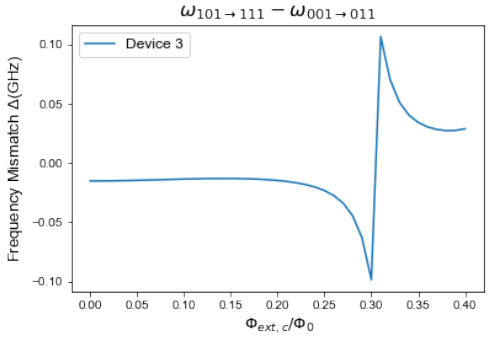

Figure 4.16: The frequency mismatch for Device 3.

The figure indicates that by tuning $\Phi_{ext,c}/\Phi_0$ to around 0.3, higher values of Δ^{111} can be realized. This finding is instrumental in setting the stage for the effective realization of the CZ gate, affirming the selected transition as a robust pathway for gate implementation in our device. The following is simulated using the Hamiltonian parameters of Device 3.

4.6.2. LEAKAGE AND FIDELITY OF TWO-QUBIT GATE

In Section 3.3.3, the driving Hamiltonian has been discussed. By adding this item into the Eq. (3.21), The Hamiltonian of the FXTFX system is:

$$\hat{H} = \sum_i \hat{H}_i + \sum_{i\neq j} \hat{H}_{ij} + \hat{H}_{\text{drive}}, \quad \{i,j\} \in \{1,2,c\} \tag{4.9}$$

First, only the on-resonant in-phase pulse is applied, ω_d being the transition frequency from $|101\rangle$ to $|111\rangle$ state and $\lambda = 0$. Here, I use Device 3 to evaluate the leakage and fidelity.

The driving amplitude depends on the value of the frequency mismatches Δ^{111}, and has the relationship: $\Omega/2\pi \ll \Delta^{111}$. Δ^{111} is equal to 0.106 GHz with the Hamiltonian parameters for Device 3 and $\Phi_{ext,c}/\Phi_0 = 0.31$. Here, we set the drive amplitude as $\Omega/2\pi =$ 15MHz initially and the corresponding gate time $\tau_g = 66$ ns.

Fig. 4.17a illustrates the time-dependent population dynamics of the states $|101\rangle$ and $|111\rangle$ during the execution of the CZ gate operation. Starting in the $|101\rangle$ state, the system undergoes a coherent transition to the $|111\rangle$ state due to the Rabi drive (with a maximum population of around 0.970 in the $|111\rangle$ state). Subsequently, the system returns to its original state, completing the CZ operation.

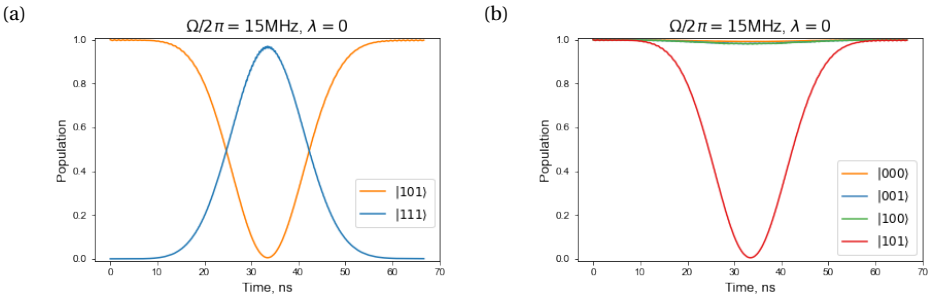

Figure 4.17: (a) Population of the states $|101\rangle$ and $|111\rangle$ during the two-qubit gate with $\Omega/2\pi = 15$MHz, $\lambda = 0$ as a function of time when the initial state is $|101\rangle$. (b) Population dynamics of states $|000\rangle$, $|100\rangle$, $|001\rangle$, $|101\rangle$ under the influence of a drive pulse designed to excite the $|101\rangle$ state to the $|111\rangle$state.

4

STATE FIDELITY

We can also get the population of computational states for the two-qubit gate with $\Omega/2\pi = 15$MHz, $\lambda = 0$ as a function of time, as shown in Fig. 4.17b.

The figure depicts the time evolution of the populations of each computational state in the presence of drive pulse. In the idealized situation, the drive pulse would exclusively act on the $|101\rangle$ state, transitioning its population from 1 to 0 and then returning it back to 1 by the end of the pulse. Simultaneously, the populations of other computational states would remain unperturbed, maintaining their population at 1 throughout the entire pulse duration.

As mentioned earlier, the population of state $|101\rangle$ performs almost perfectly. Meanwhile, the other three computational states $|000\rangle$, $|100\rangle$ and $|001\rangle$ have very minor population fluctuations. Although they exhibit a deviation from the initial population, this is small and these populations revert to their original value of 1 at the end of the gate time. This implies that the overall magnitude of the leakage is minimal, indicating robustness in our gate operation. The temporary fluctuations in states $|000\rangle$, $|100\rangle$ and $|001\rangle$ could be attributed to various factors, including the imperfections in the drive pulse, unintended resonances, or cross-talk between qubit states.

Table 4.10 illustrates the state fidelity values computed post-operation. These high fidelity values, particularly being close to 1. Despite slight transient deviations, the system largely operates as expected.

	$\|000\rangle$	$\|100\rangle$	$\|001\rangle$	$\|101\rangle$
State Fidelity	0.9997	0.9993	0.9996	0.9989

Table 4.10: The state fidelity values for computational states.

ACCUMULATED PHASE

For our CZ gate implementation, which relies on the Rabi oscillation between the $|101\rangle$ and $|111\rangle$ states to introduce a 180° phase shift. In order to verify if the process generates the corresponding phase shift, calculating the accumulated phase θ is necessary.

Eq. (4.10) expresses the formula of the acquired phase, which is computed from the individual phases ϕ_{ijk} accumulated by the $|ijk\rangle$ state, and should achieve the value π for CZ gate.

$$\theta = \phi_{000} - \phi_{100} - \phi_{001} + \phi_{101} = \pi + 2\pi k, \quad k \in \mathbb{Z} \tag{4.10}$$

Fig. 4.18 presents the evolution of the accumulated phase of our CZ gate operation as a function of gate time. By the end of the gate time, the accumulated phase is close to π. Achieving this phase value ensures the introduction of the desired π phase shift, which is essential for the effective realization of our CZ gate.

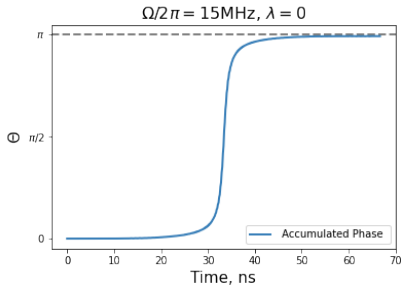

Figure 4.18: The accumulated phase θ during the gate time.

GATE FIDELITY

After having considered state fidelity and phase accumulation in our quantum system, we can evaluate quantum gate performance, usually in terms of gate fidelity. This fidelity indicates how closely the operation of our implemented quantum gate matches the target operation.

The two-qubit gate fidelity can be defined as [62, 75]

$$\mathcal{F} = \frac{1}{n(n+1)} \left[Tr(\hat{\mathcal{U}}^\dagger \hat{\mathcal{U}}) + \left| Tr(\hat{\mathcal{U}}^\dagger \hat{\mathcal{U}}_{\text{ideal}}) \right|^2 \right] \tag{4.11}$$

where n is the dimension of the computational subspace, which is 4 for our two-qubit gate system. $\hat{\mathcal{U}}$ is the implemented unitary operation described by our quantum system and $\hat{\mathcal{U}}_{\text{ideal}}$ is the ideal unitary operation of the process. For CZ gate, $\hat{\mathcal{U}}_{\text{ideal}} = \mathbf{U_{CZ}}$ and the matrix of $\mathbf{U_{CZ}}$ can be found in Eq. (3.28)

With the above equation, the average gate fidelity can be calculated as $\mathcal{F} = 99.87\%$ with the gate time $\tau_g = 66$ ns.

DRAG APPLICATION

When comparing the system's performance without DRAG ($\lambda = 0$) to the performance with DRAG applied, we note a significant improvement in the phase coherence of the system. The DRAG modulation enhances the accumulated phase from 3.12 to a more optimal value of 3.14. This refined phase control contributes to an increased gate fidelity, with $\mathscr{F}$ reaching 99.88%, measured at a gate time (τ_g) of 66 ns.

4.6.3. SUPPRESSION OF ZZ INTERACTION

In Section 3.3.2, I introduced the formula for the ZZ interaction ζ:

$$\zeta = \frac{E_{101} - E_{001} - E_{100} + E_{000}}{\hbar} \tag{4.12}$$

Here, E_m represents the eigenenergy corresponding to the eigenstate $|m\rangle$.

As mentioned previously in Section 3.3.2, a remarkable feature of the FXTFX device is its ability to effectively suppress ZZ interaction. This suppression is clearly demonstrated in the simulated ZZ interaction data for Device 3, presented in Fig. 4.19. It is evident that ζ consistently remains below 10 kHz, thus demonstrating remarkable suppression capabilities.

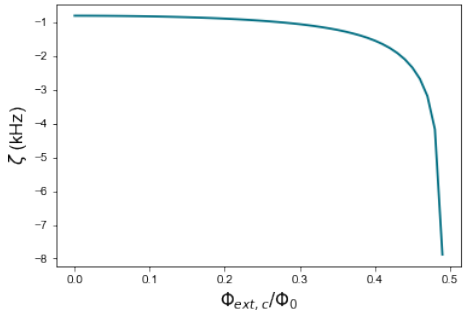

Figure 4.19: Simulated ζ as a function of the coupler flux for the FXTFX Device 3 parameters.

For a comprehensive understanding of this phenomenon, I extend the ZZ interaction ζ to fourth order, as detailed in Appendix B. The expanded interaction can be presented as:

$$\zeta = \zeta^{(2)} + \zeta^{(3)} + \zeta^{(4)} \tag{4.13}$$

The first-order correction to ζ is zero, whereas the subsequent terms are given by:

$$\zeta^{(2)} = g_{12}^2 \zeta_E^{(2)}, \qquad \zeta^{(3)} = g_{12} g_{1c} g_{2c} \zeta_E^{(3)}, \qquad \zeta^{(4)} = g_{1c}^2 g_{2c}^2 \zeta_E^{(4)} \tag{4.14}$$

Upon examining the second-order term, as detailed in Appendix B.2, we observe that $\zeta_E^{(2)}$ is negative, as shown in Fig. 4.20a. This negative value is a consequence of the energy

eigenstate $|j\rangle$ having higher energy than $|m\rangle$, resulting in negative E_{mj} values. Crucially, only direct transitions between the two fluxonium qubits contribute to $\zeta^{(2)}$ and other transitions, which are between fluxonium qubit and coupler will offset each other.

The third-order term, denoted as $\zeta^{(3)}$, which is derived in Appendix B.3, exhibits a contrasting behavior compared to the second-order term. Instead of contributing negatively, it introduces a positive value to the ZZ interaction, see Fig. 4.20a. Notably, this term not only involves g_{12}, signifying transitions between the two fluxonium qubits, but also incorporates transitions between fluxonium qubits and the coupler. Consequently, terms such as g_{1c} and g_{2c} are integral to the third-order term.

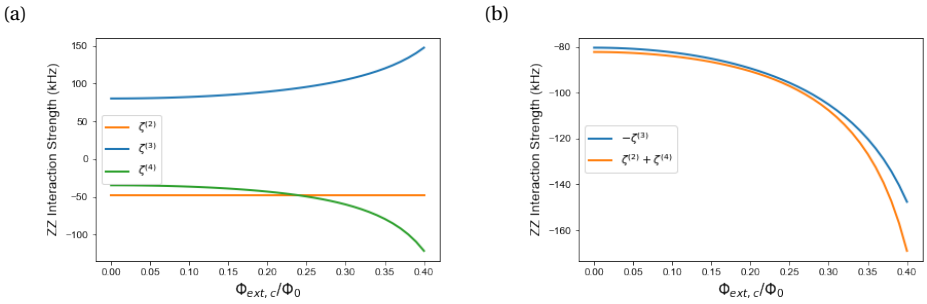

Figure 4.20: (a) The simulation result for $\zeta^{(2)}$, $\zeta^{(3)}$ and $\zeta^{(4)}$ with respect to the external flux of the coupler. (b) A comparison between the negative $\zeta^{(3)}$ term and the sum of $\zeta^{(2)}$ and $\zeta^{(4)}$ terms.

Conversely, the fourth-order term, $\zeta^{(4)}$, the derivation of which can be found in Appendix B.4. Much like the second-order term, its contribution to the ZZ interaction is negative, as depicted in Fig. 4.20a. Meanwhile, the fourth-order ZZ interaction is primarily due to transitions between the coupler and fluxonium qubits, with $g_{1c}(g_{2c})$ is much larger than g_{12} condition.

To provide a visual representation of these behaviors, I have included Fig. 4.20a, which graphically shows the simulation results for $\zeta^{(2)}$, $\zeta^{(3)}$, and $\zeta^{(4)}$ with respect to changes in the external flux of the coupler. Furthermore, Fig. 4.20b offers a useful comparison between the negative $\zeta^{(3)}$ term and the sum of $\zeta^{(2)}$ and $\zeta^{(4)}$ terms. The gap between these two lines provides a clear visualization of the total ZZ interaction, highlighting the critical mechanism by which the FXTFX system effectively mitigates ZZ interactions.

By incorporating the expressions for each order of $\zeta^{(n)}$ from Eq. (4.14) into Eq. (4.13), I obtain a comprehensive expression for ζ as follows:

$$\begin{aligned}\zeta &= g_{12}^2\zeta_E^{(2)} + g_{12}g_{1c}g_{2c}\zeta_E^{(3)} + g_{1c}^2g_{2c}^2\zeta_E^{(4)} \\ &= g_{12}^2\zeta_E^{(2)} + g_{12}g_{ic}^2\zeta_E^{(3)} + g_{ic}^4\zeta_E^{(4)}\end{aligned} \tag{4.15}$$

In this expression, I assume that g_{1c} and g_{2c} are equal, and introduce the notation g_{ic}, with $i \in \{1,2\}$, to represent the coupling strengths between fluxonium qubits and the coupler. Further insights can be gained by taking the partial derivative of Eq. (4.15) with

respect to g_{12}:

$$\frac{d\zeta}{dg_{12}} = 2g_{12}\zeta_E^{(2)} + g_{ic}^2\zeta_E^{(3)} = 0, \qquad g_{12} = \frac{-\zeta_E^{(3)}}{2\zeta_E^{(2)}}g_{ic}^2 \tag{4.16}$$

This equation provides the relationship between g_{12} and g_{ic} in minimizing ζ. When setting $\Phi_{ext,c} = 0.31\Phi_0$, the values of each order of $\zeta_E^{(n)}$ are tabulated in Table 4.11.

$\zeta_E^{(2)}$ (GHz^{-1})	$\zeta_E^{(3)}$ (GHz^{-2})	$\zeta_E^{(4)}$ (GHz^{-3})
-0.0269	0.0501	-0.0241

Table 4.11: The value of $\zeta_E^{(n)}$, $n \in 2,3,4$, at $\Phi_{ext,c} = 0.31\Phi_0$.

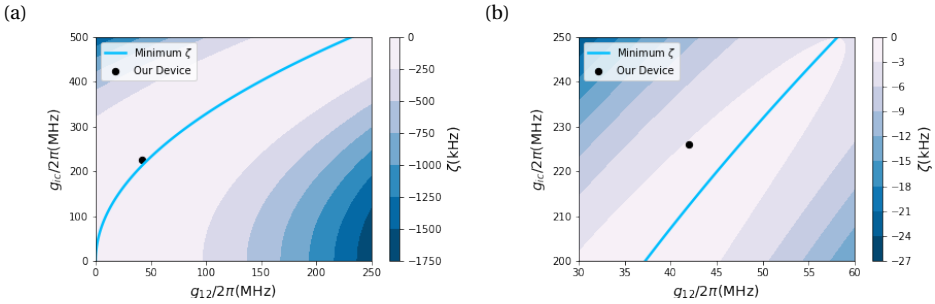

Figure 4.21: (a) Numerical simulation of ζ as a function of g_{12} and g_{ic} in Eq. (4.15) for Device 3. With the coupler, a ratio of coupling strengths in Eq. (4.16) could show the minimum ζ (blue line). Dark dot is corresponding to the coupling strengths for our device. (b) A magnified view of (a), focusing on the region around our device.

After obtaining the values presented in Table 4.11, I construct a graph illustrating the minimum achievable ζ. Within this plot, our device is represented as the dark dot. As depicted in Fig. 4.21b, this point is in proximity to the blue curve, which signifies the minimum ζ achievable with the coupler. This closeness to the curve helps to explain why our device exhibits a remarkably low ZZ interaction. Moreover, Fig. 4.21b serves as a zoomed-in visualization derived from the data presented in Table 4.11, showing that the ZZ interaction of Device 3 is maintained below 3 kHz when $\Phi_{ext,c}$ is set to $0.31\Phi_0$. This notably low ZZ interaction demonstrates the FXTFX device's effective suppression capabilities.

5

FABRICATION AND MEASUREMENT

In this chapter, we will discuss the details of measurement results for fabricated FXTFX devices.

5.1. FABRICATION

The chip was fabricated by Figen, and its optical image of the wire-bonded chip can be seen in Fig. 5.1a. Wirebonding is the interconnect technology to ground the device and also provides a pathway for electrical signals to and from the chip.

For a more detailed perspective, refer to Fig. 5.1b. This is a false-colored optical micrograph of a single FXTFX device. Each fluxonium qubit, is accompanied by a flux line (purple line) and a charge line(green line). The readout line is positioned at the base of the fluxonium qubit (dark blue part). The tunable transmon is solely equipped with the flux line.

5.2. MEASUREMENT SETUP

Superconducting qubits, as depicted in Fig. 5.1a operate under extremely cold conditions, specifically at milli-Kelvin (mK) temperatures. Achieving this low temperature is paramount to observing dominant quantum effects, which would otherwise be obscured by thermal noise.

5.2.1. COOLING MECHANISM

A specialized cooling system was used. Measurements were performed using a BlueFors LD400 dilution refrigerator (DR), which is capable of cooling the superconducting device to an environmental temperature of 8 mK. This ensures an environment conducive

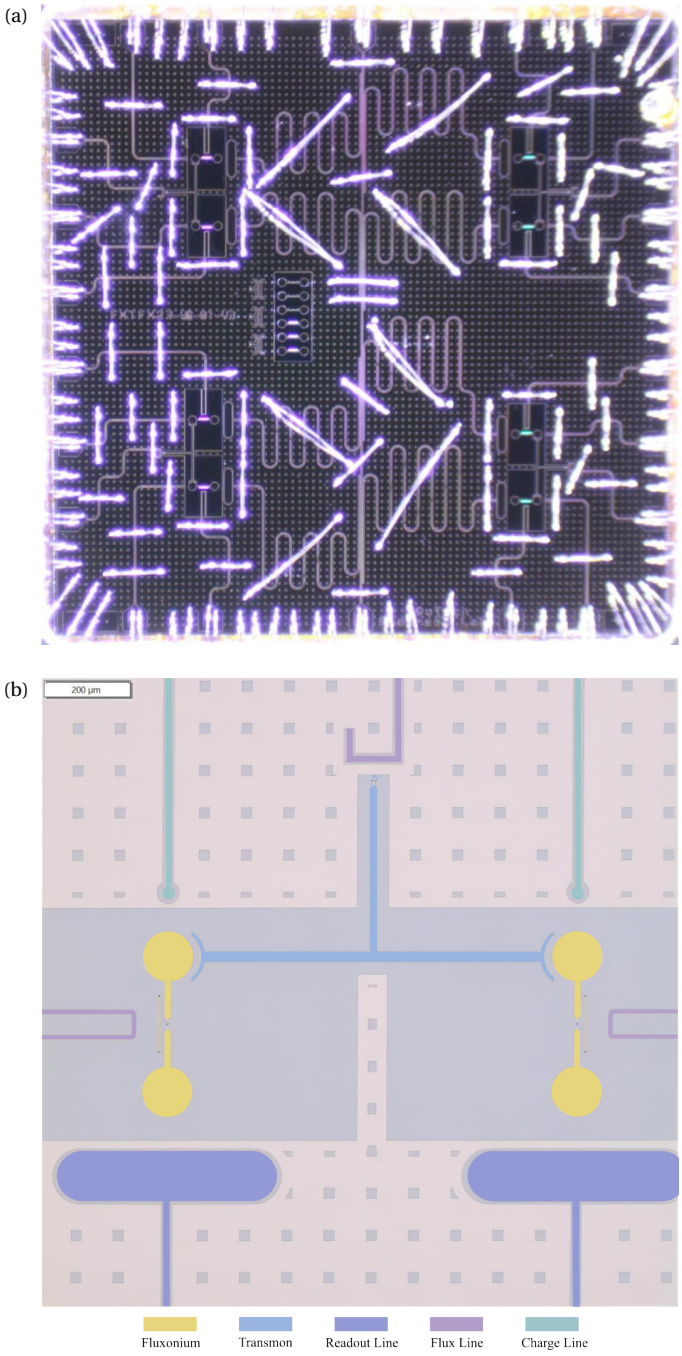

Figure 5.1: (a) The layout of chip after wire bonding. (b) False-colored optical micrograph of the two fluxonium qubits and the transmon along with readout resonators, charge lines, and flux lines.

for the qubits to function optimally. An illustration of the measurement setup is provided in Appendix D. For clarity and simplicity, the schematic diagram shows only the measurement setup associated with a single FXTFX device on the chip.

5.3. RESULT

The measurement results were done by Eugene Y. Huang, Taryn V. Stefanski and Siddharth Singh.

5.3.1. RESONATOR CHARACTERISATION

Before diving into more complex measurements or operations with the qubits, it's crucial to ensure that basic elements of the chip, like the readout resonators, are working as expected. The Vector Network Analyzer (VNA) is employed for this purpose. By sweeping across a broad frequency range, it confirms the resonance frequencies of the resonators. When an input signal V_{in} is sent into the resonator, the relationship between the input and output V_{out} is denoted by the equation: $V_{out} = S_{21} V_{in}$.

Notably, when the readout signal resonates with one of the readout resonators, S_{21} displays a distinct dip in its amplitude, indicating the resonance occurrence. Fig. 5.2 illustrates the magnitude response of S_{21} for the first designed readout resonator. By examining this distinct dip, the resonance frequency of the resonator is discernible. In this case, the resonant frequency of the first resonator is pinpointed at 5.819 GHz.

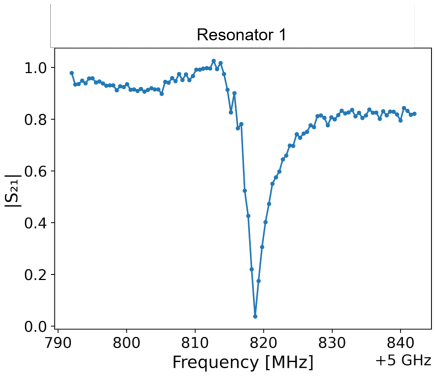

Figure 5.2: Measured S21 versus frequency trace of for Resonator 1.

Detailed magnitude responses of S_{21} for the other resonators are furnished in Appendix E.1. Furthermore, a comprehensive list of resonance frequencies for all resonators is presented in Table 5.1.

The difference between the simulated and measured frequencies (from 0.23 GHz to 0.35 GHz) can be attributed to the kinetic inductance energy of NbTiN being higher than anticipated in the simulation. This results in a lower resonant frequency, consistent with

Resonator	1	2	4	5	7	8	10	11
Simulated Frequency(GHz)	6.109	6.474	6.765	7.087	5.751	5.437	5.186	4.778
Measured Frequency(GHz)	5.819	6.133	6.427	6.728	5.476	5.178	4.945	4.544
Discrepancy(GHz)	0.29	0.341	0.338	0.359	0.275	0.259	0.241	0.234

Table 5.1: Comparison of simulated and measured frequencies across the eight resonators.

the relationship between inductance and frequency as shown in Eq. (4.2).

Following the resonance frequency confirmation, some additional evaluation is essential. The power scan is to assess the functionality ("liveness") of a qubit and find the maximum readout amplitude. Furthermore, the flux scan and two-tone spectroscopy are essential in ascertaining the sweet pot for fluxonium qubits.

5.3.2. QUBIT CHARACTERISATION

Having established the readout parameters, we proceeded with qubit spectroscopy, an essential step in the measurement characterisation of a qubit system. This involves sending microwave pulses across a range that encompasses the expected qubit transition frequency, while the qubit readout frequency remains fixed. The qubit frequency is determined by identifying the peak in the readout signal.

Once the qubit frequency is discerned, Rabi oscillation is performed to calibrate the π-pulse amplitude. This amplitude represents the microwave amplitude required to transition the qubit from the ground state $|0\rangle$ to the excited state $|1\rangle$.

Upon completion of these preliminary steps, we have established the foundational parameters to control the qubit. Subsequently, three key measurements are performed for qubits at the sweet spot: the relaxation time (T_1), the Ramsey experiments (T_2^*), and the Echo experiments (T_2^{echo}).

Figs. E.3a and E.3b in Appendix E.2 show the T_1 time for the fluxonium qubit 7 and fluxonium qubit 8 of Device 3 within the chip, which is approximately 16.54 μs and 28.9 μs. This time indicates the average time for a qubit to relax from its excited state $|1\rangle$ to the ground state $|0\rangle$. In comparison, the tmon qubit 9 in Device 3 has a notably shorter T_1 time of 330 ns, as illustrated in Fig. E.3c (Appendix E.2). Additionally, the echo dephasing times, T_2^{echo}, for these fluxonium qubits are provided in **??** and Fig. E.4b, measured to be 8.47 μs for qubit 7 and 8.55 μs for qubit 8. The T_2^{echo} time provides the dephasing characteristics of the qubits, indicating their ability to maintain coherence over time.

When implementing the CZ gate, we need to use the Rabi oscillation to drive the $|101\rangle$ to $|111\rangle$ transition. Hence, we don't want the tmon to decay during the middle of the operation, which means the T_1 time of tmon is particularly important. Similarly, the coherence time T_2 of fluxonium qubits is essential. CZ operation is fundamentally dependent on the accumulation of specific phases. If fluxonium qubits lose coherence quickly, the accumulated phase might not be correct, leading to gate errors.

For successful quantum operations, it's crucial that the gate operation time be significantly shorter than the shortest T_1 and T_2 times among the three qubits. As discussed in Section 3.3, gate fidelity varies with the gate operation time. For a gate time of 66 ns, we achieve a fidelity of $\mathscr{F} = 99.88\%$. This operation time is within the coherence times of the fluxonium qubit. However, potential risk arise from the short T_1 of tmon and there's an increased likelihood of the tmon decaying mid-operation, potentially introducing errors.

The coherence times of our fluxonium qubit and tmon impose limits on the lengths of our quantum gate operations. However, we're optimistic about our future prospects in this direction. As a precedent, Xin, a fellow master student, has successfully optimized the driving pulse and readout, resulting in significantly enhanced coherence times of $T_1 = 74\ \mu s$ and $T_2^{echo} = 20.7\ \mu s$. As for the tmon, considering that this is our first fabrication and measurement of this new qubit, there is still enough space for optimization to extend its T_1 time, whether in terms of design, fabrication, pulse shaping or otherwise.

6

CONCLUSION AND OUTLOOK

6.1. SUMMARY OF MAIN WORK

In this thesis, we have introduced a configuration that combines the coherence advantages of fluxonium qubits with the tunability and high-frequency attributes of tunable transmon qubits, presenting a promising avenue for the development of robustness, large-scale quantum computing architectures.

In Chapter 3, we delved deep into the derivation of theoretical formula describing the coupling strengths between qubits in the FXTFX device. We embarked on the design of the tunable transmon, named tmon in Chapter 4. Subsequently, it was integrated with two fluxonium qubits previously designed by Figen. Through evaluations using the derived coupling strength formulas for the FXTFX system, we made iterative improvements concerning the shape of the device and the inter-qubit distances. Our finalized design adopted a strongly coupled FXTFX device, characterized by coupling strengths of $g_{12}/2\pi$=42MHz, and $g_{1c}/2\pi = g_{2c}/2\pi = 226$ MHz.

Upon determining the Hamiltonian parameters, we employed Scqubits package to assess the device's ZZ interaction, which we successfully maintained below 10kHz with strong coupling strengths. A thorough frequency mismatch Δ evaluation between $|101\rangle$ to $|111\rangle$ and $|101\rangle$ to $|201\rangle$ /$|102\rangle$ led us to opt for the $|101\rangle$ to $|111\rangle$ transition to implement the CZ gate. For fabricating complex fluxonium qubits, this transition is nearly insensitive to changes in the Hamiltonian parameters of fluxonium qubits.

Performance evaluation, a critical procedure in our study, was conducted by assessing state fidelity across four computational states, accumulated phase investigations, and gate fidelity. An enlightening discovery was the role of DRAG pulses in enhancing gate performance, ultimately achieving a gate fidelity of 99.88% with a gate time of 66ns.

6.2. OUTLOOK

While we have successfully designed and simulated the CZ gate with a fidelity of 99.88%, there remain promising avenues for further enhancements.

1. **Drive Pulse Optimization and Error Analysis:** Our attempts at adjusting the value of λ have yet to push the gate fidelity to 99.9%. A detailed error source analysis in the future can offer insights into optimizing the drive pulse further. Furthermore, drawing from Xin's use of Optimized Randomized Benchmarking for Immediate Tune-up (ORBIT) to improve single-qubit gate fidelity, similar methods can be used to bolster two-qubit gate performance.

2. **Improving Qubit Coherence:** Optical micrographs show that impurities are present on the chip surface as well as that the flux lines are too far away from the tunable transmon, thereby constraining gate performance and increasing error rate. To address these issues, a rigorous fabrication process is crucial. By adopting cleaner fabrication techniques and optimizing the geometry of the flux line to decrease its distance from the tunable transmon, we can aim to enhance the coherence times of our qubits.

3. **Asymmetric Josephson Junctions in Tmon:** Our current design employs symmetric Josephson junctions in the tunable transmon, providing a broad frequency spectrum. This assists in identifying optimal frequencies for CZ gate implementation and the suppression of ZZ interactions. For future designs, asymmetric Josephson junctions may be considered. They can potentially allow a wider flux range in the Tmon for the CZ gate. However, achieving the right balance of asymmetry between junctions might necessitate more intricate design and fabrication processes, increasing potential error sources.

By identifying current limitations and developing potential solutions, we hope to further improve two-qubit gate fidelity. The development of our FXTFX device is an important step forward in the evolving field of quantum computing, especially in the area of two-qubit gate implementations.

Appendices

A

Additional Content for Circuit Quantization

A.1. Transition Matrix

$$\mathbf{M}^{-1} = \begin{bmatrix} \frac{1}{2} & \frac{1}{2} & 0 & 0 & 0 \\ -\frac{1}{2} & \frac{1}{2} & 0 & 0 & 0 \\ 0 & 0 & 1 & 0 & 0 \\ 0 & 0 & 0 & \frac{1}{2} & \frac{1}{2} \\ 0 & 0 & 0 & -\frac{1}{2} & \frac{1}{2} \end{bmatrix} \quad (\mathbf{M}^{-1})^T = \begin{bmatrix} \frac{1}{2} & -\frac{1}{2} & 0 & 0 & 0 \\ \frac{1}{2} & \frac{1}{2} & 0 & 0 & 0 \\ 0 & 0 & 1 & 0 & 0 \\ 0 & 0 & 0 & \frac{1}{2} & -\frac{1}{2} \\ 0 & 0 & 0 & \frac{1}{2} & \frac{1}{2} \end{bmatrix} \tag{A.1}$$

A.2. Details of Inverse Matrix Values

To calculate the concrete values for the coupling strength, we can use the following formulas for $\widetilde{\mathbf{C}}^{-1}[1,3]$, $\widetilde{\mathbf{C}}^{-1}[3,4]$ and $\widetilde{\mathbf{C}}^{-1}[1,4]$

$$\begin{aligned} \mathbf{C}^{-1}[1,3] &= \frac{(C_{1tc}\mathbb{C}_{22} - \mathbb{C}_{11}C_{1bc}) + C_{1t1b}(C_{1bc} - C_{1tc})}{\mathbb{C}_{11}\mathbb{C}_{22}\mathbb{C}_{33}} \\ \mathbf{C}^{-1}[3,4] &= \frac{(C_{c2t}\mathbb{C}_{55} - \mathbb{C}_{44}C_{c2b}) + C_{2t2b}(C_{c2b} - C_{c2t})}{\mathbb{C}_{33}\mathbb{C}_{44}\mathbb{C}_{55}} \\ \mathbf{C}^{-1}[1,4] &= \frac{(C_{c2t}\mathbb{C}_{55} - C_{c2b}\mathbb{C}_{44})(C_{1t1b}(C_{1bc} - C_{1tc}) - \mathbb{C}_{11}C_{1bc} + C_{1tc}\mathbb{C}_{22})}{\mathbb{C}_{11}\mathbb{C}_{22}\mathbb{C}_{33}\mathbb{C}_{44}\mathbb{C}_{55}} \\ &\quad + \frac{C_{2t2b}(C_{c2b} - C_{c2t})(\mathbb{C}_{22}C_{1tc} - \mathbb{C}_{11}C_{1bc})}{\mathbb{C}_{11}\mathbb{C}_{22}\mathbb{C}_{33}\mathbb{C}_{44}\mathbb{C}_{55}} \end{aligned} \tag{A.2}$$

B

DERIVATION FOR ZZ COUPLING RATE

B.1. HAMILTONIAN

We start from the Hamiltonian, which could be found in Section 3.2.2, the interaction Hamiltonian for the FXTFX device can be described as

$$\begin{aligned} H_{int} &= H_{1c} + H_{2c} + H_{12} \\ &= \hbar g_{1c}\hat{n}_1\hat{n}_c + \hbar g_{2c}\hat{n}_2\hat{n}_c + \hbar g_{12}\hat{n}_1\hat{n}_2 \end{aligned} \tag{B.1}$$

Here, $\hat{n}_i$, $i \in \{1,2,c\}$ is the charge operator. In the harmonic Oscillator basis with creation and annihilation operator $\hat{a}^\dagger(\hat{a})$, it can be written as[62]

$$\begin{aligned} \hat{n}_\mathrm{f} &= \frac{i}{\sqrt{2}}\left(\frac{E_L}{8E_C}\right)^{\frac{1}{4}}(\hat{a}^\dagger - \hat{a}) \\ \hat{n}_\mathrm{t} &= \frac{i}{\sqrt{2}}\left(\frac{E_J}{8E_C}\right)^{\frac{1}{4}}(\hat{a}^\dagger - \hat{a}) \end{aligned} \tag{B.2}$$

$\hat{n}_\mathrm{f}$ is fluxonium charge operator and $\hat{n}_\mathrm{t}$ is for transmon qubit.

Hence, Eq. (B.1) can be rewritten as

$$\begin{aligned} H_{int} = &-\sum_{i=1,2}\frac{\hbar g_{ic}}{4\sqrt{2}}\left(\frac{E_{Li}E_{Jc}}{E_{Ci}E_{Cc}}\right)^{\frac{1}{4}}(\hat{a_i}^\dagger - \hat{a}_i)(\hat{a_c}^\dagger - \hat{a}_c) \\ &-\frac{\hbar g_{12}}{4\sqrt{2}}\left(\frac{E_{L1}E_{L2}}{E_{C1}E_{C2}}\right)^{\frac{1}{4}}(\hat{a_1}^\dagger - \hat{a}_1)(\hat{a_2}^\dagger - \hat{a}_2) \end{aligned} \tag{B.3}$$

The ZZ interaction ζ is given by

$$\zeta = \frac{E_{101} - E_{001} - E_{100} + E_{000}}{\hbar} \tag{B.4}$$

B.2. SECOND ORDER TERMS

Second order corrections are given by Eq. (3.32)

$$E_m^{(2)} = \sum_{j \neq m} \frac{|V_{mj}|^2}{E_{mj}^{(0)}} \tag{B.5}$$

The eigenstates and its corresponding contributions are shown in the below table

m	j	Contributions
$\|101\rangle$	$\|000\rangle$	$\frac{1}{E_{101\to000}}$
	$\|002\rangle$	$\frac{2}{E_{101\to002}}$
	$\|200\rangle$	$\frac{2}{E_{101\to200}}$
	$\|202\rangle$	$\frac{4}{E_{101\to202}}$
$\|100\rangle$	$\|201\rangle$	$\frac{2}{E_{100\to201}}$
	$\|001\rangle$	$\frac{1}{E_{100\to001}}$
$\|001\rangle$	$\|102\rangle$	$\frac{2}{E_{001\to102}}$
	$\|100\rangle$	$\frac{1}{E_{001\to100}}$
$\|000\rangle$	$\|101\rangle$	$\frac{1}{E_{000\to101}}$

Table B.1: Second order terms for ZZ interaction.

Here, $E_{m\to j} = E_m - E_j$, $E_{101\to000} = -E_{000\to101}$ and $E_{100\to001} = -E_{001\to100}$. Hence, only computational eigenstates evolve the energy shift will no contribution for the ZZ interaction.

The second order ZZ interaction can be summarized as

$$\begin{aligned}\zeta^{(2)} &= \frac{g_{12}^2}{32}\left[\frac{E_{L1}E_{L2}}{E_{C1}E_{C2}}\right]^{\frac{1}{2}}\left(\frac{1}{E_{101\to002}} + \frac{1}{E_{101\to200}} + \frac{2}{E_{101\to202}} - \frac{1}{E_{100\to201}} - \frac{1}{E_{001\to102}}\right) \\ &= g_{12}^2\zeta_E^{(2)}\end{aligned} \tag{B.6}$$

B.3. THIRD ORDER TERMS

Third order corrections are given by Eq. (3.33)

$$E_m^{(3)} = \sum_{j,k \neq m} \frac{V_{mj}V_{jk}V_{km}}{E_{mj}^{(0)}E_{mk}^{(0)}} \tag{B.7}$$

B

m	j	k	Contributions
$\|101\rangle$	$\|211\rangle$	$\|112\rangle$	$\frac{4}{E_{101\to211}E_{101\to112}}$
		$\|110\rangle$	$\frac{2}{E_{101\to211}E_{101\to110}}$
		$\|202\rangle$	$\frac{4}{E_{101\to211}E_{101\to202}}$
		$\|200\rangle$	$\frac{2}{E_{101\to211}E_{101\to200}}$
	$\|011\rangle$	$\|112\rangle$	$\frac{2}{E_{101\to011}E_{101\to112}}$
		$\|110\rangle$	$\frac{1}{E_{101\to011}E_{101\to110}}$
		$\|002\rangle$	$\frac{2}{E_{101\to011}E_{101\to002}}$
		$\|000\rangle$	$\frac{1}{E_{101\to011}E_{101\to000}}$
	$\|112\rangle$	$\|202\rangle$	$\frac{4}{E_{101\to112}E_{101\to202}}$
		$\|002\rangle$	$\frac{2}{E_{101\to112}E_{101\to002}}$
	$\|110\rangle$	$\|200\rangle$	$\frac{2}{E_{101\to110}E_{101\to200}}$
		$\|000\rangle$	$\frac{1}{E_{101\to110}E_{101\to000}}$
$\|100\rangle$	$\|210\rangle$	$\|111\rangle$	$\frac{2}{E_{100\to210}E_{100\to111}}$
		$\|201\rangle$	$\frac{2}{E_{100\to210}E_{100\to201}}$
	$\|010\rangle$	$\|111\rangle$	$\frac{1}{E_{100\to010}E_{100\to111}}$
		$\|001\rangle$	$\frac{1}{E_{100\to010}E_{100\to001}}$
	$\|111\rangle$	$\|201\rangle$	$\frac{2}{E_{100\to111}E_{100\to201}}$
		$\|001\rangle$	$\frac{1}{E_{100\to111}E_{100\to001}}$
$\|001\rangle$	$\|012\rangle$	$\|111\rangle$	$\frac{2}{E_{001\to012}E_{001\to111}}$
		$\|102\rangle$	$\frac{2}{E_{001\to012}E_{001\to102}}$
	$\|010\rangle$	$\|100\rangle$	$\frac{1}{E_{001\to010}E_{001\to100}}$
		$\|111\rangle$	$\frac{1}{E_{001\to010}E_{001\to111}}$
	$\|111\rangle$	$\|102\rangle$	$\frac{2}{E_{001\to111}E_{001\to102}}$
		$\|100\rangle$	$\frac{1}{E_{001\to111}E_{001\to100}}$
$\|000\rangle$	$\|110\rangle$	$\|011\rangle$	$\frac{1}{E_{000\to110}E_{000\to011}}$
		$\|101\rangle$	$\frac{1}{E_{000\to110}E_{000\to101}}$
	$\|011\rangle$	$\|101\rangle$	$\frac{1}{E_{000\to011}E_{000\to101}}$

Table B.2: Third order terms for ZZ interaction.

Here, we only illustrated $j \neq k$ items, for instance, when $m = |101\rangle, j = |112\rangle, k = |211\rangle$, its contribution is the same as $m = |101\rangle, j = |211\rangle, k = |112\rangle$ element.

We can calculate the sum of above elements, named $\sum E^{-1}$ and the final result for $\zeta^{(3)}$

is

$$\begin{aligned}\zeta^{(3)} &= -\frac{g_{12}g_{1c}g_{2c}}{128\sqrt{2}}\left[\frac{E_{L1}E_{L2}E_{Jc}}{E_{C1}E_{C2}E_{Cc}}\right]^{\frac{1}{2}}\sum E^{-1}\times 2 \\ &= g_{12}g_{1c}g_{2c}\zeta_E^{(3)}\end{aligned} \tag{B.8}$$

B.4. FOURTH ORDER TERMS

The fourth order corrections are given by

$$E_m^{(4)} = \sum_{j,k,l\neq m}\frac{V_{mj}V_{jk}V_{kl}V_{lm}}{E_{mj}^{(0)}E_{mk}^{(0)}E_{ml}^{(0)}} - \sum_{j,k\neq m}\frac{|V_{mj}|^2|V_{mk}|^2}{(E_{mj}^{(0)})^2E_{mk}^{(0)}} \tag{B.9}$$

Because $g_{12} \ll g_{ic}$, we omit the g_{12} term in the derivation of the fourth-order perturbation. Besides, there are two types of terms in are denoted by I and II and listed in Tables B.3 and B.4. Here, we only illustrated $j \neq l$ items, for instance, when $m = |101\rangle$, $j = |211\rangle$, $k = |121\rangle$, $l = |112\rangle$, its contribution is the same as $m = |101\rangle$, $j = |112\rangle$, $k = |121\rangle$, $l = |211\rangle$ element.

Table B.3: Table:I. Fourth order corrections for $|101\rangle$ states.

m	j	k	l	Contributions
$\|101\rangle$	$\|211\rangle$	$\|121\rangle$	$\|112\rangle$	$\frac{8g_{1c}^2g_{2c}^2}{E_{101\to211}E_{101\to121}E_{101\to112}}\times 2$
		$\|202\rangle$	$\|112\rangle$	$\frac{4g_{1c}^2g_{2c}^2}{E_{101\to211}E_{101\to202}E_{101\to112}}\times 2$
		$\|222\rangle$	$\|112\rangle$	$\frac{8g_{1c}^2g_{2c}^2}{E_{101\to211}E_{101\to222}E_{101\to112}}\times 2$
		$\|121\rangle$	$\|110\rangle$	$\frac{4g_{1c}^2g_{2c}^2}{E_{101\to211}E_{101\to121}E_{101\to110}}\times 2$
		$\|200\rangle$	$\|110\rangle$	$\frac{2g_{1c}^2g_{2c}^2}{E_{101\to211}E_{101\to200}E_{101\to110}}\times 2$
		$\|220\rangle$	$\|110\rangle$	$\frac{4g_{1c}^2g_{2c}^2}{E_{101\to211}E_{101\to220}E_{101\to110}}\times 2$
		$\|121\rangle$	$\|011\rangle$	$\frac{4g_{1c}^4}{E_{101\to211}E_{101\to121}E_{101\to011}}\times 2$ offset
	$\|211\rangle$	$\|200\rangle$	$\|211\rangle$	$\frac{2g_{1c}^2g_{2c}^2}{E_{101\to211}E_{101\to200}E_{101\to211}}$
		$\|220\rangle$	$\|211\rangle$	$\frac{4g_{1c}^2g_{2c}^2}{E_{101\to211}E_{101\to220}E_{101\to211}}$
		$\|202\rangle$	$\|211\rangle$	$\frac{4g_{1c}^2g_{2c}^2}{E_{101\to211}E_{101\to202}E_{101\to211}}$
		$\|222\rangle$	$\|211\rangle$	$\frac{8g_{1c}^2g_{2c}^2}{E_{101\to211}E_{101\to222}E_{101\to211}}$
		$\|121\rangle$	$\|211\rangle$	$\frac{8g_{1c}^4}{E_{101\to211}E_{101\to121}E_{101\to211}}$ offset
	$\|011\rangle$	$\|121\rangle$	$\|112\rangle$	$\frac{4g_{1c}^2g_{2c}^2}{E_{101\to011}E_{101\to121}E_{101\to112}}\times 2$
		$\|022\rangle$	$\|112\rangle$	$\frac{4g_{1c}^2g_{2c}^2}{E_{101\to011}E_{101\to022}E_{101\to112}}\times 2$

Continued on next page

B

Table B.3 – continued from previous page

m	j	k	l	Contributions
		$\|002\rangle$	$\|112\rangle$	$\frac{2g_{1c}^2 g_{2c}^2}{E_{101\to011}E_{101\to002}E_{101\to112}} \times 2$
		$\|121\rangle$	$\|110\rangle$	$\frac{2g_{1c}^2 g_{2c}^2}{E_{101\to011}E_{101\to121}E_{101\to110}} \times 2$
		$\|000\rangle$	$\|110\rangle$	$\frac{g_{1c}^2 g_{2c}^2}{E_{101\to011}E_{101\to000}E_{101\to110}} \times 2$
		$\|020\rangle$	$\|110\rangle$	$\frac{2g_{1c}^2 g_{2c}^2}{E_{101\to011}E_{101\to020}E_{101\to110}} \times 2$
	$\|011\rangle$	$\|121\rangle$	$\|011\rangle$	$\frac{2g_{1c}^4}{E_{101\to011}E_{101\to121}E_{101\to011}}$ offset
		$\|000\rangle$	$\|011\rangle$	$\frac{g_{1c}^2 g_{2c}^2}{E_{101\to011}E_{101\to000}E_{101\to011}}$
		$\|002\rangle$	$\|011\rangle$	$\frac{2g_{1c}^2 g_{2c}^2}{E_{101\to011}E_{101\to002}E_{101\to011}}$
		$\|020\rangle$	$\|011\rangle$	$\frac{2g_{1c}^2 g_{2c}^2}{E_{101\to011}E_{101\to020}E_{101\to011}}$
		$\|022\rangle$	$\|011\rangle$	$\frac{4g_{1c}^2 g_{2c}^2}{E_{101\to011}E_{101\to022}E_{101\to011}}$
	$\|112\rangle$	$\|121\rangle$	$\|110\rangle$	$\frac{4g_{2c}^4}{E_{101\to112}E_{101\to121}E_{101\to110}} \times 2$ offset
	$\|112\rangle$	$\|121\rangle$	$\|112\rangle$	$\frac{8g_{2c}^4}{E_{101\to112}E_{101\to121}E_{101\to112}}$ offset
		$\|002\rangle$	$\|112\rangle$	$\frac{2g_{1c}^2 g_{2c}^2}{E_{101\to112}E_{101\to002}E_{101\to112}}$
		$\|022\rangle$	$\|112\rangle$	$\frac{4g_{1c}^2 g_{2c}^2}{E_{101\to112}E_{101\to022}E_{101\to112}}$
		$\|202\rangle$	$\|112\rangle$	$\frac{4g_{1c}^2 g_{2c}^2}{E_{101\to112}E_{101\to202}E_{101\to112}}$
		$\|222\rangle$	$\|112\rangle$	$\frac{8g_{1c}^2 g_{2c}^2}{E_{101\to112}E_{101\to222}E_{101\to112}}$
	$\|110\rangle$	$\|121\rangle$	$\|110\rangle$	$\frac{2g_{2c}^4}{E_{101\to110}E_{101\to121}E_{101\to110}}$ offset
		$\|200\rangle$	$\|110\rangle$	$\frac{2g_{1c}^2 g_{2c}^2}{E_{101\to110}E_{101\to200}E_{101\to110}}$
		$\|220\rangle$	$\|110\rangle$	$\frac{4g_{1c}^2 g_{2c}^2}{E_{101\to110}E_{101\to220}E_{101\to110}}$
		$\|020\rangle$	$\|110\rangle$	$\frac{2g_{1c}^2 g_{2c}^2}{E_{101\to110}E_{101\to020}E_{101\to110}}$
		$\|000\rangle$	$\|110\rangle$	$\frac{g_{1c}^2 g_{2c}^2}{E_{101\to110}E_{101\to000}E_{101\to110}}$

Table B.4: Table:I. Fourth order corrections for $|100\rangle$, $|001\rangle$ and $|000\rangle$ states.

m	j	k	l	Contributions
$\|100\rangle$	$\|210\rangle$	$\|120\rangle$	$\|010\rangle$	$\frac{4g_{1c}^4}{E_{100\to210}E_{100\to120}E_{100\to010}} \times 2$ offset
		$\|120\rangle$	$\|111\rangle$	$\frac{4g_{1c}^2 g_{2c}^2}{E_{100\to210}E_{100\to120}E_{100\to111}} \times 2$
		$\|221\rangle$	$\|111\rangle$	$\frac{4g_{1c}^2 g_{2c}^2}{E_{100\to210}E_{100\to221}E_{100\to111}} \times 2$

Continued on next page

Table B.4 – continued from previous page

m	j	k	l	Contributions
		$\|201\rangle$	$\|111\rangle$	$\frac{2g_{1c}^2 g_{2c}^2}{E_{100\to210}E_{100\to201}E_{100\to111}} \times 2$
	$\|210\rangle$	$\|120\rangle$	$\|210\rangle$	$\frac{8g_{1c}^4}{E_{100\to210}E_{100\to120}E_{100\to210}}$ offset
		$\|221\rangle$	$\|210\rangle$	$\frac{4g_{1c}^2 g_{2c}^2}{E_{100\to210}E_{100\to221}E_{100\to210}}$
		$\|201\rangle$	$\|210\rangle$	$\frac{2g_{1c}^2 g_{2c}^2}{E_{100\to210}E_{100\to201}E_{100\to210}}$
	$\|010\rangle$	$\|120\rangle$	$\|111\rangle$	$\frac{2g_{1c}^2 g_{2c}^2}{E_{100\to010}E_{100\to120}E_{100\to111}} \times 2$
		$\|021\rangle$	$\|111\rangle$	$\frac{2g_{1c}^2 g_{2c}^2}{E_{100\to010}E_{100\to021}E_{100\to111}} \times 2$
		$\|001\rangle$	$\|111\rangle$	$\frac{g_{1c}^2 g_{2c}^2}{E_{100\to010}E_{100\to001}E_{100\to111}} \times 2$
	$\|010\rangle$	$\|120\rangle$	$\|010\rangle$	$\frac{2g_{1c}^4}{E_{100\to010}E_{100\to120}E_{100\to010}}$ offset
		$\|021\rangle$	$\|010\rangle$	$\frac{2g_{1c}^2 g_{2c}^2}{E_{100\to010}E_{100\to021}E_{100\to010}}$
		$\|001\rangle$	$\|010\rangle$	$\frac{g_{1c}^2 g_{2c}^2}{E_{100\to010}E_{100\to001}E_{100\to010}}$
	$\|111\rangle$	$\|001\rangle$	$\|111\rangle$	$\frac{g_{1c}^2 g_{2c}^2}{E_{100\to111}E_{100\to001}E_{100\to111}}$
		$\|221\rangle$	$\|111\rangle$	$\frac{4g_{1c}^2 g_{2c}^2}{E_{100\to111}E_{100\to221}E_{100\to111}}$
		$\|201\rangle$	$\|111\rangle$	$\frac{2g_{1c}^2 g_{2c}^2}{E_{100\to111}E_{100\to201}E_{100\to111}}$
		$\|021\rangle$	$\|111\rangle$	$\frac{2g_{1c}^2 g_{2c}^2}{E_{100\to111}E_{100\to021}E_{100\to111}}$
		$\|122\rangle$	$\|111\rangle$	$\frac{4g_{2c}^4}{E_{100\to111}E_{100\to122}E_{100\to111}}$ offset
		$\|102\rangle$	$\|111\rangle$	$\frac{2g_{2c}^4}{E_{100\to111}E_{100\to102}E_{100\to111}}$ offset
		$\|120\rangle$	$\|111\rangle$	$\frac{2g_{2c}^4}{E_{100\to111}E_{100\to120}E_{100\to111}}$ offset
$\|001\rangle$	$\|012\rangle$	$\|122\rangle$	$\|111\rangle$	$\frac{4g_{1c}^2 g_{2c}^2}{E_{001\to012}E_{001\to122}E_{001\to111}} \times 2$
		$\|102\rangle$	$\|111\rangle$	$\frac{2g_{1c}^2 g_{2c}^2}{E_{001\to012}E_{001\to102}E_{001\to111}} \times 2$
		$\|021\rangle$	$\|111\rangle$	$\frac{4g_{1c}^2 g_{2c}^2}{E_{001\to012}E_{001\to021}E_{001\to111}} \times 2$
		$\|021\rangle$	$\|010\rangle$	$\frac{4g_{2c}^4}{E_{001\to012}E_{001\to021}E_{001\to010}} \times 2$ offset
	$\|012\rangle$	$\|122\rangle$	$\|012\rangle$	$\frac{4g_{1c}^2 g_{2c}^4}{E_{001\to012}E_{001\to122}E_{001\to012}}$
		$\|102\rangle$	$\|012\rangle$	$\frac{2g_{1c}^2 g_{2c}^2}{E_{001\to012}E_{001\to102}E_{001\to012}}$
		$\|021\rangle$	$\|012\rangle$	$\frac{8g_{2c}^2}{E_{001\to012}E_{001\to021}E_{001\to012}}$ offset
	$\|010\rangle$	$\|120\rangle$	$\|111\rangle$	$\frac{2g_{1c}^2 g_{2c}^2}{E_{001\to010}E_{001\to120}E_{001\to111}} \times 2$
		$\|021\rangle$	$\|111\rangle$	$\frac{2g_{1c}^2 g_{2c}^2}{E_{001\to010}E_{001\to021}E_{001\to111}} \times 2$
		$\|100\rangle$	$\|111\rangle$	$\frac{g_{1c}^2 g_{2c}^2}{E_{001\to010}E_{001\to100}E_{001\to111}} \times 2$
	$\|010\rangle$	$\|120\rangle$	$\|010\rangle$	$\frac{2g_{1c}^2 g_{2c}^2}{E_{001\to010}E_{001\to120}E_{001\to010}}$

Continued on next page

B

Table B.4 – continued from previous page

m	j	k	l	Contributions
		$\|021\rangle$	$\|010\rangle$	$\frac{2g_{1c}^4}{E_{001\to010}E_{001\to021}E_{001\to010}}$ offset
		$\|100\rangle$	$\|010\rangle$	$\frac{g_{1c}^2 g_{2c}^2}{E_{001\to010}E_{001\to100}E_{001\to010}}$
	$\|111\rangle$	$\|100\rangle$	$\|111\rangle$	$\frac{g_{1c}^2 g_{2c}^2}{E_{001\to111}E_{001\to100}E_{001\to111}}$
		$\|221\rangle$	$\|111\rangle$	$\frac{4g_{1c}^4}{E_{001\to111}E_{001\to221}E_{001\to111}}$ offset
		$\|201\rangle$	$\|111\rangle$	$\frac{2g_{1c}^4}{E_{001\to111}E_{001\to201}E_{001\to111}}$ offset
		$\|021\rangle$	$\|111\rangle$	$\frac{2g_{1c}^4}{E_{001\to111}E_{001\to021}E_{001\to111}}$ offset
		$\|122\rangle$	$\|111\rangle$	$\frac{4g_{1c}^2 g_{2c}^2}{E_{001\to111}E_{001\to122}E_{001\to111}}$
		$\|102\rangle$	$\|111\rangle$	$\frac{2g_{1c}^2 g_{2c}^2}{E_{001\to111}E_{001\to102}E_{001\to111}}$
		$\|120\rangle$	$\|111\rangle$	$\frac{2g_{1c}^2 g_{2c}^2}{E_{001\to111}E_{001\to120}E_{001\to111}}$
$\|000\rangle$	$\|110\rangle$	$\|020\rangle$	$\|011\rangle$	$\frac{2g_{1c}^2 g_{2c}^2}{E_{000\to110}E_{000\to020}E_{000\to011}} \times 2$
		$\|121\rangle$	$\|011\rangle$	$\frac{2g_{1c}^2 g_{2c}^2}{E_{000\to110}E_{000\to121}E_{000\to011}} \times 2$
		$\|101\rangle$	$\|011\rangle$	$\frac{g_{1c}^2 g_{2c}^2}{E_{000\to110}E_{000\to101}E_{000\to011}} \times 2$
	$\|110\rangle$	$\|101\rangle$	$\|110\rangle$	$\frac{g_{1c}^2 g_{2c}^2}{E_{000\to110}E_{000\to101}E_{000\to110}}$
		$\|121\rangle$	$\|110\rangle$	$\frac{2g_{1c}^2 g_{2c}^2}{E_{000\to110}E_{000\to121}E_{000\to110}}$
		$\|200\rangle$	$\|110\rangle$	$\frac{2g_{1c}^4}{E_{000\to110}E_{000\to200}E_{000\to110}}$ offset
		$\|020\rangle$	$\|110\rangle$	$\frac{2g_{1c}^4}{E_{000\to110}E_{000\to020}E_{000\to110}}$ offset
		$\|220\rangle$	$\|110\rangle$	$\frac{4g_{1c}^4}{E_{000\to110}E_{000\to220}E_{000\to110}}$ offset
	$\|011\rangle$	$\|101\rangle$	$\|011\rangle$	$\frac{g_{1c}^2 g_{2c}^2}{E_{000\to011}E_{000\to101}E_{000\to011}}$
		$\|121\rangle$	$\|011\rangle$	$\frac{2g_{1c}^2 g_{2c}^2}{E_{000\to011}E_{000\to121}E_{000\to011}}$
		$\|002\rangle$	$\|011\rangle$	$\frac{2g_{2c}^4}{E_{000\to011}E_{000\to002}E_{000\to011}}$ offset
		$\|020\rangle$	$\|011\rangle$	$\frac{2g_{2c}^4}{E_{000\to011}E_{000\to020}E_{000\to011}}$ offset
		$\|022\rangle$	$\|011\rangle$	$\frac{4g_{2c}^4}{E_{000\to011}E_{000\to022}E_{000\to011}}$ offset

Table B.5: Table:II. Fourth order corrections.

m	j	k	Contributions
$\|101\rangle$	$\|211\rangle$	$\|011\rangle$	$\frac{2g_{1c}^4}{(E_{101\to211})^2 E_{101\to011}}$ offset

Continued on next page

Table B.5 – continued from previous page

m	j	k	Contributions
		$\|112\rangle$	$\frac{4g_{1c}^2 g_{2c}^2}{(E_{101\to 211})^2 E_{101\to 112}}$
		$\|110\rangle$	$\frac{2g_{1c}^2 g_{2c}^2}{(E_{101\to 211})^2 E_{101\to 110}}$
		$\|211\rangle$	$\frac{4g_{1c}^4}{(E_{101\to 211})^3}$ offset
	$\|011\rangle$	$\|211\rangle$	$\frac{2g_{1c}^4}{(E_{101\to 011})^2 E_{101\to 211}}$ offset
		$\|112\rangle$	$\frac{2g_{1c}^2 g_{2c}^2}{(E_{101\to 011})^2 E_{101\to 112}}$
		$\|110\rangle$	$\frac{g_{1c}^2 g_{2c}^2}{(E_{101\to 011})^2 E_{101\to 110}}$
		$\|011\rangle$	$\frac{g_{1c}^4}{(E_{101\to 011})^3}$ offset
	$\|112\rangle$	$\|211\rangle$	$\frac{4g_{1c}^2 g_{2c}^2}{(E_{101\to 112})^2 E_{101\to 211}}$
		$\|110\rangle$	$\frac{2g_{1c}^2 g_{2c}^2}{(E_{101\to 112})^2 E_{101\to 011}}$
		$\|110\rangle$	$\frac{2g_{2c}^4}{(E_{101\to 112})^2 E_{101\to 110}}$ offset
		$\|112\rangle$	$\frac{4g_{2c}^4}{(E_{101\to 112})^3}$ offset
	$\|110\rangle$	$\|211\rangle$	$\frac{2g_{1c}^2 g_{2c}^2}{(E_{101\to 110})^2 E_{101\to 211}}$
		$\|011\rangle$	$\frac{g_{1c}^2 g_{2c}^2}{(E_{101\to 110})^2 E_{101\to 011}}$
		$\|112\rangle$	$\frac{2g_{2c}^4}{(E_{101\to 110})^2 E_{101\to 112}}$ offset
		$\|110\rangle$	$\frac{g_{2c}^4}{(E_{101\to 110})^3}$ offset
$\|100\rangle$	$\|210\rangle$	$\|010\rangle$	$\frac{2g_{1c}^4}{(E_{100\to 210})^2 E_{100\to 010}}$ offset
		$\|111\rangle$	$\frac{2g_{1c}^2 g_{2c}^2}{(E_{100\to 210})^2 E_{100\to 111}}$
		$\|210\rangle$	$\frac{4g_{1c}^4}{(E_{100\to 210})^3}$ offset
	$\|010\rangle$	$\|210\rangle$	$\frac{2g_{1c}^4}{(E_{100\to 010})^2 E_{100\to 210}}$ offset
		$\|111\rangle$	$\frac{g_{1c}^2 g_{2c}^2}{(E_{100\to 010})^2 E_{100\to 111}}$
		$\|010\rangle$	$\frac{g_{1c}^4}{(E_{100\to 010})^3}$ offset
	$\|111\rangle$	$\|210\rangle$	$\frac{2g_{1c}^2 g_{2c}^2}{(E_{100\to 111})^2 E_{100\to 210}}$
		$\|010\rangle$	$\frac{g_{1c}^2 g_{2c}^2}{(E_{100\to 111})^2 E_{100\to 010}}$
		$\|111\rangle$	$\frac{g_{2c}^4}{(E_{100\to 111})^3}$ offset
$\|001\rangle$	$\|012\rangle$	$\|010\rangle$	$\frac{2g_{2c}^4}{(E_{001\to 012})^2 E_{001\to 010}}$ offset
		$\|111\rangle$	$\frac{2g_{1c}^2 g_{2c}^2}{(E_{001\to 012})^2 E_{001\to 111}}$
		$\|012\rangle$	$\frac{4g_{2c}^4}{(E_{001\to 012})^3}$ offset
	$\|010\rangle$	$\|012\rangle$	$\frac{2g_{2c}^4}{(E_{001\to 010})^2 E_{001\to 012}}$ offset

Continued on next page

Table B.5 – continued from previous page

m	j	k	Contributions
		$\|111\rangle$	$\frac{g_{1c}^2 g_{2c}^2}{(E_{001\to010})^2 E_{001\to111}}$
		$\|010\rangle$	$\frac{g_{2c}^4}{(E_{001\to010})^3}$ offset
	$\|111\rangle$	$\|012\rangle$	$\frac{2g_{1c}^2 g_{2c}^2}{(E_{001\to111})^2 E_{001\to012}}$
		$\|010\rangle$	$\frac{g_{1c}^2 g_{2c}^2}{(E_{001\to111})^2 E_{001\to010}}$
		$\|111\rangle$	$\frac{g_{1c}^4}{(E_{001\to111})^3}$ offset
$\|000\rangle$	$\|110\rangle$	$\|011\rangle$	$\frac{g_{1c}^2 g_{2c}^2}{(E_{000\to110})^2 E_{000\to011}}$
		$\|110\rangle$	$\frac{g_{1c}^4}{(E_{000\to110})^3}$ offset
	$\|011\rangle$	$\|110\rangle$	$\frac{g_{1c}^2 g_{2c}^2}{(E_{000\to011})^2 E_{000\to110}}$
		$\|011\rangle$	$\frac{g_{2c}^4}{(E_{000\to011})^3}$ offset

From the above table we can find the g_{ic}^4, $i \in 1,2$ items will no contribution to the total fourth order ZZ interaction because the equal and opposite items will offset them.

We can calculate the sum of above effective elements, named $\sum E^{-1}$ and the final result for $\zeta^{(4)}$ is

$$\begin{aligned}\zeta^{(4)} &= \frac{g_{1c}^2 g_{2c}^2}{1024}\left[\frac{E_{L1}E_{L2}E_{Jc}^2}{E_{C1}E_{C2}E_{Cc}^2}\right]^{\frac{1}{2}}\sum E^{-1} \\ &= g_{1c}^2 g_{2c}^2 \zeta_E^{(4)}\end{aligned} \tag{B.10}$$

C

COUPLING QUALITY AND DECAY RATE

This appendix details the calculations for the coupling quality factor (Q_c) and the decay rate (κ) of the resonators used in this project. We begin by revisiting the formula for the coupling quality factor of a half-wavelength resonator:

$$Q_c = \frac{\pi}{\omega_r^2 Z_0 Z_r C_k^2} \tag{C.1}$$

In this formula, Z_0 and Z_r are the characteristic impedances of the feedline and the resonator, respectively, set to 45 Ω. The angular frequency of the resonator is denoted by ω_r, and C_k represents the coupling capacitance between the resonator and the feedline. For the purposes of this appendix, we focus on the derivation process for Resonator 10.

The dressed frequency f_0 of Resonator 10 is 5.186 MHz, which gives the value of $\omega_r/2\pi$. Utilizing ANSYS-Q3D for electromagnetic simulation, the following Maxwell capacitance matrix is obtained:

	g_wb	trace_cavity10	trace_TL
g_wb	3244.07410	-1735.59339	-1288.93441
trace_cavity10	-1735.59339	1774.99038	-37.71266
trace_TL	-1288.93441	-37.71266	1327.98780

Figure C.1: The capacitance matrix for resonator 10 with the feedline. The unit of capacitance is fF.

From this matrix, I extract the coupling capacitance value, $C_k = 37.71$fF. Substituting all these values into Equation C.1, I calculate the coupling quality factor, Q_c, to be approximately 1029.74, a dimensionless parameter.

The next step is to calculate the decay rate (κ), which can be determined using the formula:

$$\kappa = \frac{f_0}{Q_c} \tag{C.2}$$

Applying this formula, the decay rate for Resonator 10 is found to be 5.03 MHz. This methodology can be similarly applied to calculate the Q_c and κ for the other resonators in the circuit.

D

MEASUREMENT SETUP

The FXTFX chip is located at the bottom, encased in a Mu-metal cylinder, to effectively shield the superconducting device from potentially disruptive magnetic fields. Additionally:

- Attenuators are installed to filter out excess thermal photons from higher-temperature stages, thereby minimizing noise.
- Eccosorb filters, are employed to absorb thermal radiation noise.
- Low-pass filters aid in reducing high-frequency noise that might interfere with the operation of qubit.
- A circulator, a unique nonreciprocal microwave device[76], is positioned at the coldest section of the cryostat. Its function is twofold: directing the readout in a singular direction and shielding the qubits from noise propagating from the output line.

The high-electron-mobility transistors (HEMT) play a pivotal role as the primary readout electronics. Their function is to amplify the faint signals produced by the qubits, preparing them for transmission to the room-temperature equipment. Post this, the output line undergoes another round of amplification using room-temperature amplifiers.

Outside the cryostat, the amplified signals encounter an IQ mixer for downconversion. Subsequently, these signals are transmitted to Ultra High Frequency Quantum Analyzer (UHFQA). Notably, the UHFQA also has the capability to generate signals that are fed into the device's input line.

For signal generation specific to the charge line, the multi-channel High-density Arbitrary Waveform Generator (HDAWG) is utilized. Where the required frequency exceeds

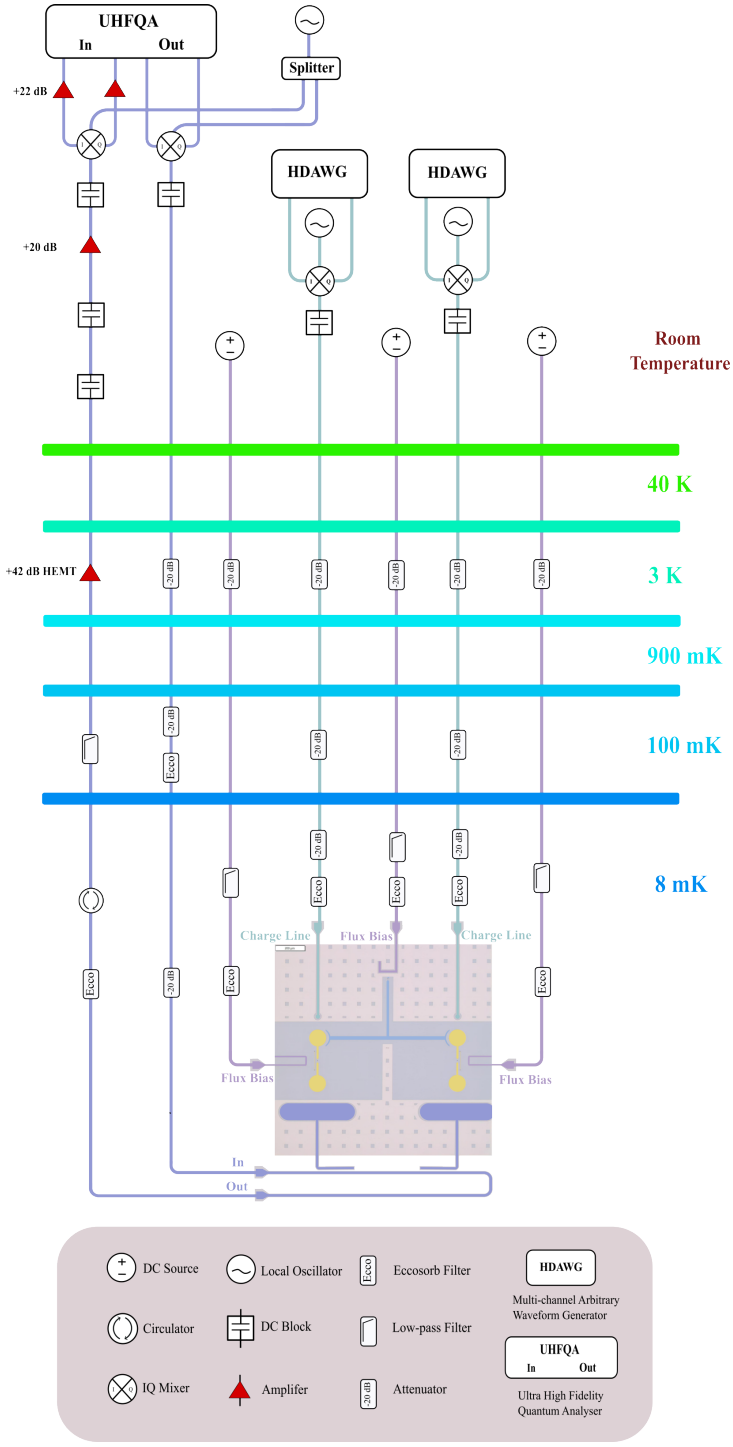

Figure D.1: Measurement setup for a single FXTFX device.

the HDAWG upper limit, the signal from the HDAWG is combined with an RF source originating from the local oscillator (LO). Conversely, flux line signals can directly be generated by DC sources to ensure operations occur at the desired energy levels.

E

Additional Measurement Results

E.1. Readout Resonator Spectroscopy

Here, we illustrate the magnitude response of S_{21} for all designed readout resonators.

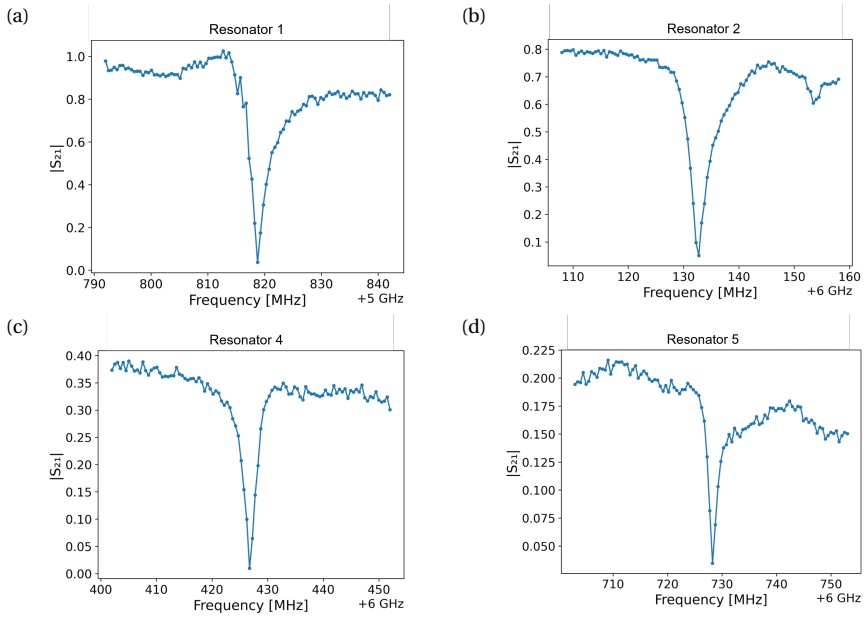

Figure E.1: Measured S21 vs frequency trace of for Resonator1, 2, 4, 5.

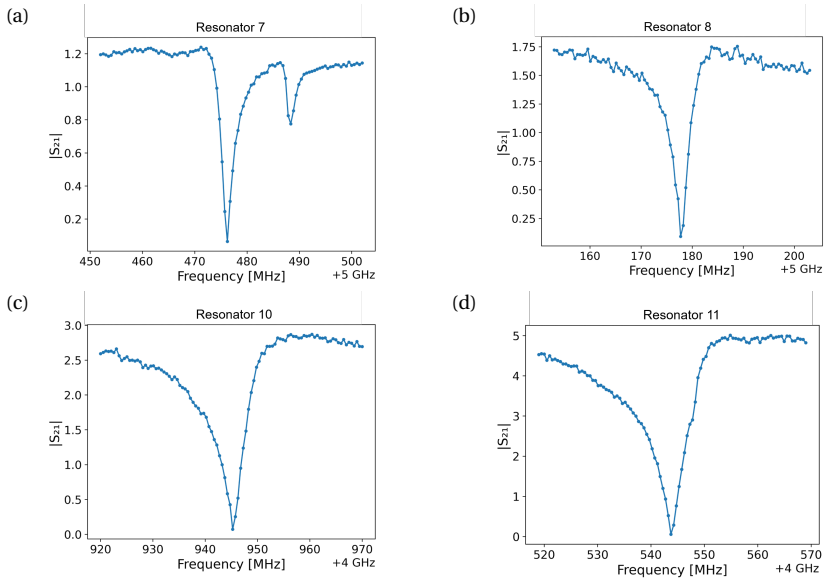

Figure E.2: Measured S21 vs frequency trace of for Resonator 7, 8, 10, 11.

E.2. QUBIT SPECTROSCOPY

Here, we show the T_1 for fluxonium qubits 7, 8, and tmon 9.

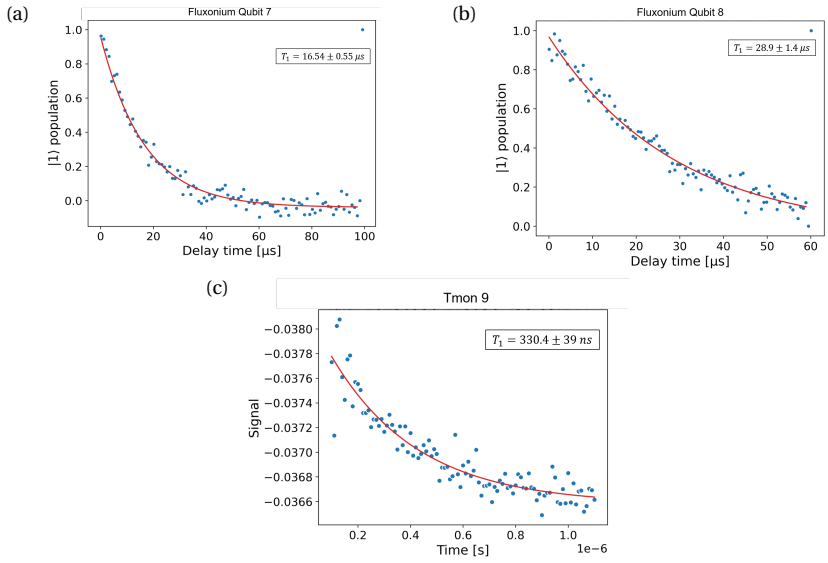

Figure E.3: T_1 measurement for fluxonium qubits 7, 8 and tmon 9 (d) T_1 measurement for Tmon 9.

The following figures are T_2^{echo} for fluxonium qubit 7 and 8.

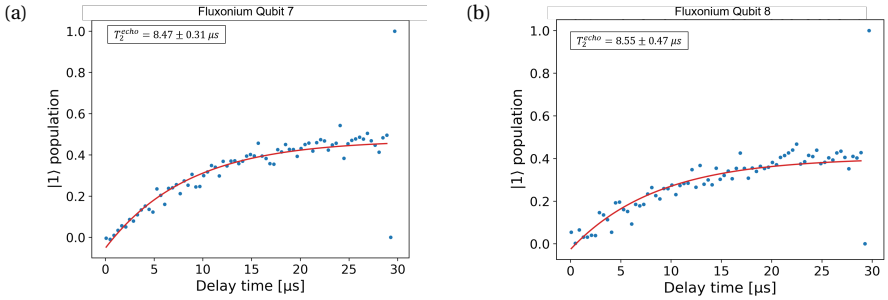

Figure E.4: Echo experiment for fluxonium qubits 7 and 8.

BIBLIOGRAPHY

[1] Barbara M Terhal, Jonathan Conrad, and Christophe Vuillot. “Towards scalable bosonic quantum error correction”. In: *Quantum Science and Technology* 5.4 (2020), p. 043001.

[2] Jens Koch et al. “Charge-insensitive qubit design derived from the Cooper pair box”. In: *Phys. Rev. A* 76 (4 2007), p. 042319.

[3] WC Smith et al. “Superconducting circuit protected by two-Cooper-pair tunneling”. In: *npj Quantum Information* 6.1 (2020), p. 8.

[4] Vladimir E Manucharyan et al. “Fluxonium: Single cooper-pair circuit free of charge offsets”. In: *Science* 326.5949 (2009), pp. 113–116.

[5] Aaron Somoroff et al. “Millisecond coherence in a superconducting qubit”. In: *arXiv preprint arXiv:2103.08578* (2021).

[6] Feng Bao et al. “Fluxonium: an alternative qubit platform for high-fidelity operations”. In: *Physical Review Letters* 129.1 (2022), p. 010502.

[7] Konstantin N Nesterov et al. “Microwave-activated controlled-Z gate for fixed-frequency fluxonium qubits”. In: *Physical Review A* 98.3 (2018), p. 030301.

[8] Quentin Ficheux et al. “Fast logic with slow qubits: microwave-activated controlled-Z gate on low-frequency fluxoniums”. In: *Physical Review X* 11.2 (2021), p. 021026.

[9] Leon Ding et al. “High-Fidelity, Frequency-Flexible Two-Qubit Fluxonium Gates with a Transmon Coupler”. In: *arXiv preprint arXiv:2304.06087* (2023).

[10] Juan I Cirac and Peter Zoller. “Quantum computations with cold trapped ions”. In: *Physical review letters* 74.20 (1995), p. 4091.

[11] Diego Porras and J Ignacio Cirac. “Effective quantum spin systems with trapped ions”. In: *Physical review letters* 92.20 (2004), p. 207901.

[12] Thomas Monz et al. “Realization of the quantum Toffoli gate with trapped ions”. In: *Physical review letters* 102.4 (2009), p. 040501.

[13] Farhang Haddadfarshi and Florian Mintert. “High fidelity quantum gates of trapped ions in the presence of motional heating”. In: *New Journal of Physics* 18.12 (2016), p. 123007.

[14] Dominik Schrader et al. “Neutral atom quantum register”. In: *Physical Review Letters* 93.15 (2004), p. 150501.

[15] Dieter Jaksch et al. “Fast quantum gates for neutral atoms”. In: *Physical Review Letters* 85.10 (2000), p. 2208.

[16] L Isenhower et al. “Demonstration of a neutral atom controlled-NOT quantum gate”. In: *Physical review letters* 104.1 (2010), p. 010503.

[17] Loïc Henriet et al. “Quantum computing with neutral atoms”. In: *Quantum* 4 (2020), p. 327.

[18] Ye Wang et al. “Single-qubit quantum memory exceeding ten-minute coherence time”. In: *Nature Photonics* 11.10 (2017), pp. 646–650.

[19] Christopher Monroe and Jungsang Kim. “Scaling the ion trap quantum processor”. In: *Science* 339.6124 (2013), pp. 1164–1169.

[20] Frank Arute et al. “Quantum supremacy using a programmable superconducting processor”. In: *Nature* 574.7779 (2019), pp. 505–510.

[21] Eric Hyyppä et al. “Unimon qubit”. In: *Nature Communications* 13.1 (2022), p. 6895.

[22] Rami Barends et al. “Superconducting quantum circuits at the surface code threshold for fault tolerance”. In: *Nature* 508.7497 (2014), pp. 500–503.

[23] Jian-Qiang You and Franco Nori. “Atomic physics and quantum optics using superconducting circuits”. In: *Nature* 474.7353 (2011), pp. 589–597.

[24] Peter Groszkowski and Jens Koch. “Scqubits: a Python package for superconducting qubits”. In: *Quantum* 5 (2021), p. 583.

[25] David Brown and EP Hamilton. “Electromechanical energy conversion”. In: (1985).

[26] Royce KP Zia, Edward F Redish, and Susan R McKay. “Making sense of the Legendre transform”. In: *American Journal of Physics* 77.7 (2009), pp. 614–622.

[27] Alexandre Blais et al. “Circuit quantum electrodynamics”. In: *Reviews of Modern Physics* 93.2 (2021), p. 025005.

[28] Steven M Girvin. “Circuit QED: superconducting qubits coupled to microwave photons”. In: *Quantum machines: measurement and control of engineered quantum systems* (2014), pp. 113–256.

[29] Marlan O Scully and M Suhail Zubairy. *Quantum optics*. 1999.

[30] Brian David Josephson. “Possible new effects in superconductive tunnelling”. In: *Physics letters* 1.7 (1962), pp. 251–253.

[31] Yasunobu Nakamura, Yu A Pashkin, and JS Tsai. “Coherent control of macroscopic quantum states in a single-Cooper-pair box”. In: *nature* 398.6730 (1999), pp. 786–788.

[32] Vincent Bouchiat et al. “Quantum coherence with a single Cooper pair”. In: *Physica Scripta* 1998.T76 (1998), p. 165.

[33] Irinel Chiorescu et al. “Coherent quantum dynamics of a superconducting flux qubit”. In: *Science* 299.5614 (2003), pp. 1869–1871.

[34] TP Orlando et al. “Superconducting persistent-current qubit”. In: *Physical Review B* 60.22 (1999), p. 15398.

[35] John M Martinis. “Superconducting phase qubits”. In: *Quantum information processing* 8 (2009), pp. 81–103.

[36] Michael Tinkham. *Introduction to superconductivity*. Courier Corporation, 2004.

[37] Konstantin K Likharev. *Dynamics of Josephson junctions and circuits*. Routledge, 2022.

[38] Yuriy Makhlin, Gerd Schön, and Alexander Shnirman. “Quantum-state engineering with Josephson-junction devices”. In: *Reviews of modern physics* 73.2 (2001), p. 357.

[39] Z.K.Minev et al. “Qiskit Metal: An Open-Source Framework for Quantum Device Design and Analysis”. In: (2021). DOI: 10.5281/zenodo.6891761.

[40] MD Hutchings et al. “Tunable superconducting qubits with flux-independent coherence”. In: *Physical Review Applied* 8.4 (2017), p. 044003.

[41] JE Mooij et al. “Josephson persistent-current qubit”. In: *Science* 285.5430 (1999), pp. 1036–1039.

[42] Philip Krantz et al. “A quantum engineer’s guide to superconducting qubits”. In: *Applied physics reviews* 6.2 (2019).

[43] Long B Nguyen et al. “High-coherence fluxonium qubit”. In: *Physical Review X* 9.4 (2019), p. 041041.

[44] Alec Maassen Van Den Brink, AJ Berkley, and M Yalowsky. “Mediated tunable coupling of flux qubits”. In: *New Journal of Physics* 7.1 (2005), p. 230.

[45] Alexandre Blais, Alexander Maassen van den Brink, and Alexandre M Zagoskin. “Tunable coupling of superconducting qubits”. In: *Physical review letters* 90.12 (2003), p. 127901.

[46] P Bertet, CJPM Harmans, and JE Mooij. “Parametric coupling for superconducting qubits”. In: *Physical Review B* 73.6 (2006), p. 064512.

[47] Johannes Majer et al. “Coupling superconducting qubits via a cavity bus”. In: *Nature* 449.7161 (2007), pp. 443–447.

[48] Fei Yan et al. “Tunable coupling scheme for implementing high-fidelity two-qubit gates”. In: *Physical Review Applied* 10.5 (2018), p. 054062.

[49] Daniel L Campbell et al. “Modular tunable coupler for superconducting qubits”. In: *arXiv preprint arXiv:2207.06607* (2022).

[50] Ilya N Moskalenko et al. “High fidelity two-qubit gates on fluxoniums using a tunable coupler”. In: *arXiv preprint arXiv:2203.16302* (2022).

[51] Eyob A Sete et al. “Floating tunable coupler for scalable quantum computing architectures”. In: *Physical Review Applied* 15.6 (2021), p. 064063.

[52] Brooks Foxen et al. “Demonstrating a continuous set of two-qubit gates for near-term quantum algorithms”. In: *Physical Review Letters* 125.12 (2020), p. 120504.

[53] Abhinav Kandala et al. “Demonstration of a high-fidelity cnot gate for fixed-frequency transmons with engineered Z Z suppression”. In: *Physical Review Letters* 127.13 (2021), p. 130501.

[54] Hui Wang et al. “Frequency Adjustable Resonator as a Tunable Coupler for Xmon Qubits”. In: *Journal of the Physical Society of Japan* 91.10 (2022), p. 104005.

[55] AO Niskanen et al. “Quantum coherent tunable coupling of superconducting qubits”. In: *Science* 316.5825 (2007), pp. 723–726.

[56] Shaojie Yuan et al. “Spin-wave-based tunable coupler between superconducting flux qubits”. In: *Physical Review A* 107.1 (2023), p. 012434.

[57] X Li et al. “Tunable coupler for realizing a controlled-phase gate with dynamically decoupled regime in a superconducting circuit”. In: *Physical Review Applied* 14.2 (2020), p. 024070.

[58] Youngkyu Sung et al. “Realization of high-fidelity cz and z z-free iswap gates with a tunable coupler”. In: *Physical Review X* 11.2 (2021), p. 021058.

[59] Hayato Goto. “Double-transmon coupler: Fast two-qubit gate with no residual coupling for highly detuned superconducting qubits”. In: *Physical Review Applied* 18.3 (2022), p. 034038.

[60] DK Weiss et al. “Fast high-fidelity gates for galvanically-coupled fluxonium qubits using strong flux modulation”. In: *PRX Quantum* 3.4 (2022), p. 040336.

[61] Jaseung Ku et al. “Suppression of Unwanted Z Z Interactions in a Hybrid Two-Qubit System”. In: *Physical review letters* 125.20 (2020), p. 200504.

[62] Long B Nguyen et al. “Blueprint for a high-performance fluxonium quantum processor”. In: *PRX Quantum* 3.3 (2022), p. 037001.

[63] Taryn V Stefanski and Christian Kraglund Andersen. “Flux-pulse-assisted Readout of a Fluxonium Qubit”. In: *arXiv preprint arXiv:2309.17286* (2023).

[64] Figen Yilmaz et al. “Fluxonium Qubit Design and EPR analysis”. In: *Bulletin of the American Physical Society* (2023).

[65] Zachariah Peterson. “Charge-insensitive qubit design derived from the Cooper pair box”. In: (2021). URL: https://resources.altium.com/p/mysterious-50-ohm-impedance-where-it-came-and-why-we-use-it.

[66] “Coplanar Waveguide Calculator”. In: (). URL: https://www.microwaves101.com/calculators/864-coplanar-waveguide-calculator.

[67] M Checchin et al. “Measurement of the Low-Temperature Loss Tangent of High-Resistivity Silicon Using a High-Q Superconducting Resonator”. In: *Physical Review Applied* 18.3 (2022), p. 034013.

[68] Martin Göppl et al. “Coplanar waveguide resonators for circuit quantum electrodynamics”. In: *Journal of Applied Physics* 104.11 (2008).

[69] Corey Rae Harrington McRae et al. “Materials loss measurements using superconducting microwave resonators”. In: *Review of Scientific Instruments* 91.9 (2020).

[70] Qi-Ming Chen et al. “Scattering coefficients of superconducting microwave resonators. I. Transfer matrix approach”. In: *Physical Review B* 106.21 (2022), p. 214505.

[71] Andreas Wallraff et al. “Strong coupling of a single photon to a superconducting qubit using circuit quantum electrodynamics”. In: *Nature* 431.7005 (2004), pp. 162–167.

[72] Enrico Di Lorenzo. “The Maxwell Capacitance Matrix”. In: (2020). URL: https://www.fastfieldsolvers.com/PapersThe_Maxwell_Capacitance_Matrix_WP110301_R02.pdf.

[73] Rami Barends et al. “Coherent Josephson qubit suitable for scalable quantum integrated circuits”. In: *Physical review letters* 111.8 (2013), p. 080502.

[74] Shuqing Song et al. “Mitigation of critical current fluctuation of Josephson junctions in superconducting quantum circuits”. In: *Applied Physics Letters* 118.24 (2021).

[75] Line Hjortshøj Pedersen, Niels Martin Møller, and Klaus Mølmer. “Fidelity of quantum operations”. In: *Physics Letters A* 367.1-2 (2007), pp. 47–51.

[76] Baleegh Abdo et al. “High-fidelity qubit readout using interferometric directional Josephson devices”. In: *PRX Quantum* 2.4 (2021), p. 040360.